ACS NANO

www.acsnano.org

ARTICLE

Chemically Tailored Growth of 2D Semiconductors via Hybrid Metal–Organic Chemical Vapor Deposition

Zhepeng Zhang,[▽] Lauren Hoang,[▽] Marisa Hocking, Zhenghan Peng, Jenny Hu, Gregory Zaborski, Jr., Pooja D. Reddy, Johnny Dollard, David Goldhaber-Gordon, Tony F. Heinz, Eric Pop, and Andrew J. Mannix*

Cite This: *ACS Nano* 2024, 18, 25414–25424

Read Online

ACCESS | Metrics & More | Article Recommendations | Supporting Information

ABSTRACT: Two-dimensional (2D) semiconducting transition-metal dichalcogenides (TMDCs) are an exciting platform for excitonic physics and next-generation electronics, creating a strong demand to understand their growth, doping, and heterostructures. Despite significant progress in solid-source (SS-) and metal–organic chemical vapor deposition (MOCVD), further optimization is necessary to grow highly crystalline 2D TMDCs with controlled doping. Here, we report a hybrid MOCVD growth method that combines liquid-phase metal precursor deposition and vapor-phase organo-chalcogen delivery to leverage the advantages of both MOCVD and SS-CVD. Using our hybrid approach, we demonstrate WS_2 growth with tunable morphologies—from separated single-crystal domains to continuous monolayer films—on a variety of substrates, including sapphire, SiO_2, and Au. These WS_2 films exhibit narrow neutral exciton photoluminescence line widths down to 27–28 meV and room-temperature mobility up to 34–36 $cm^2 V^{-1} s^{-1}$. Through simple modifications to the liquid precursor composition, we demonstrate the growth of V-doped WS_2, $Mo_xW_{1-x}S_2$ alloys, and in-plane WS_2–MoS_2 heterostructures. This work presents an efficient approach for addressing a variety of TMDC synthesis needs on a laboratory scale.

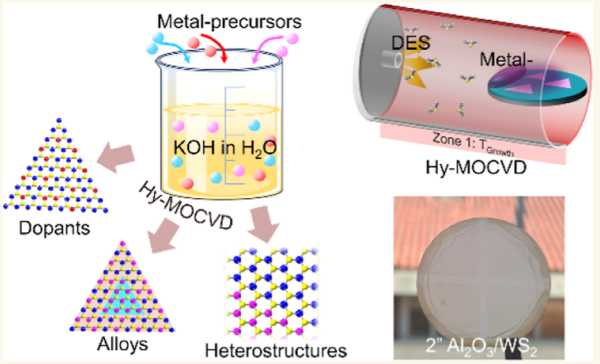

KEYWORDS: *metal–organic chemical vapor deposition, 2D semiconductor growth, transition-metal dichalcogenides, doping, alloy, WS_2, MoS_2*

Two-dimensional (2D) semiconducting transition-metal dichalcogenides (TMDCs), such as monolayer MoS_2, WS_2, and WSe_2, have emerged as attractive candidates for next-generation electronics due to their atomic-scale thickness, tunable band structure, and excellent electronic properties.[1−3] In the past decade, demonstrations of high-performance 2D TMDC-based transistors, optoelectronics, and logical circuits have escalated demand for the accurately controlled large-area growth of high-quality pure and p-/n-type-doped 2D TMDC monolayers.[4−12] Solid source chemical vapor deposition (SS-CVD) has become a popular approach for growing 2D TMDCs in laboratory settings due to its low equipment cost, flexibility, and rapid growth, enabling efficient optimization. By using SS-CVD, a wide range of 2D TMDCs, such as MoS_2,[13,14] WS_2,[6] V-doped WSe_2,[9,10] Fe-doped MoS_2,[15] and $Mo_xW_{1-x}S_2$ alloys[16] have been successfully synthesized, and wafer-scale TMDC synthesis and device fabrication have been demonstrated.[5,17]

However, further optimization for SS-CVD growth is necessary and challenging. For example, solid sources typically exhibit low sublimation rates and poor sublimation stability during the material growth process. The solid precursor is challenging to replenish midgrowth, resulting in variable stoichiometry in the reactor over time during each growth run. Small variations in the source amount and position modify the uniformity of the growth. These factors limit the tolerance

Received: February 15, 2024
Revised: August 12, 2024
Accepted: August 12, 2024
Published: September 4, 2024

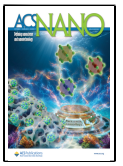

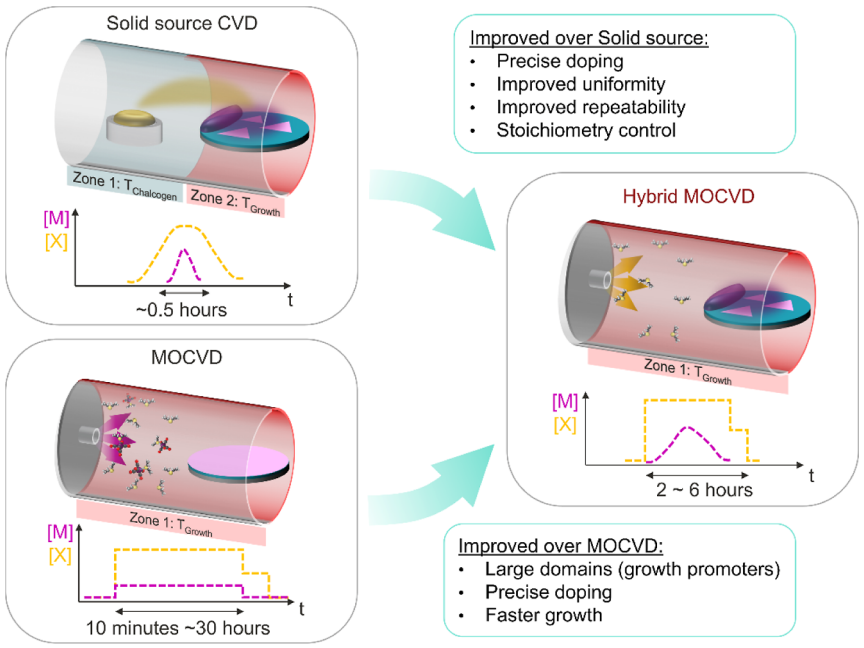

Figure 1. Principles of Hy-MOCVD. Representative schematics of the growth setups and precursor supply time profiles for conventional SS-CVD, MOCVD, and Hy-MOCVD. The *y*-axis in the time profiles stands for the active concentrations of the transition metal (M) and chalcogen (X) species. The MOCVD growth time can vary widely due to differences in growth temperature, heating methods, growth promoters, and precursor flow rates employed by various groups (as summarized in Table S2).

and controllability of SS-CVD.[18,19] Moreover, although a specific SS-CVD strategy normally works well for an individual TMDC system, a universal method for multiple-material synthesis remains underdeveloped. Even though the situation has been improved by source supply strategies[20,21] and adding promoters,[22−24] the design of state-of-the-art SS-CVD growth setups has also become increasingly complex—and, correspondingly, less accessible—for most laboratory research.

On the other hand, metal−organic CVD (MOCVD) has shown good reproducibility and large-area uniformity in 2D TMDC growth[25] at relatively low reaction temperatures (150−320 °C)[26−28] and under accurate precursor control due to the use of vapor phase metal−organic metal (M-organic) and hydride or organic chalcogen (X-organic) precursors.[25] However, to reduce carbon impurity incorporation, MOCVD often uses low precursor concentrations, resulting in slow growth rates of the 2D TMDCs. Moreover, each dopant metal−organic source requires a separate precursor supply line in the MOCVD system to avoid cross-contamination, which increases the system cost and complexity and hinders the exploration of substitutional doping. Alkali metal-based solid and gas phase growth promoters have been explored in MOCVD to increase the growth rate and decrease the nucleation density.[29−31] However, several potentially negative effects have been reported from alkali metal salts used in MOCVD, including disruption of epitaxy, the introduction of nanoscale particles, and degradation of optical and electronic properties.[32] Consequently, further research and optimization are crucial to understanding the mechanisms and optimize the use of growth promoters in MOCVD. Despite the development of MOCVD strategies to enlarge the domain size,[33] enable epitaxy,[34] and reduce the growth temperature,[26,27] more accessible and efficient MOCVD growth and doping methods are still needed.

Here, we report a hybrid MOCVD (Hy-MOCVD) growth method that delivers metal precursors and growth promoters from the solution phase and metal−organic chalcogen precursors from the vapor phase, to combine the advantages of both MOCVD and SS-CVD and realize efficient growth of multiple types of 2D TMDCs. Aqueous Hy-MOCVD precursor delivery by both spin-coating and dip-coating produces WS_2 monolayers with good controllability and uniformity. Hy-MOCVD grown WS_2 exhibits typical domain sizes of tens of micrometers, good optical quality with room temperature neutral exciton peak width down to 27−28 meV, good electronic performance with electron mobility up to 34−36 $cm^2\ V^{-1}\ s^{-1}$, and transistor on/off ratio of $>10^7$. Hy-MOCVD also enables the growth of WS_2 on diverse substrates, such as *c*-plane and *a*-plane sapphire, Si/SiO_2, and sapphire/Au. To illustrate the versatility of our Hy-MOCVD approach, we also demonstrate the facile growth of V-doped WS_2, $Mo_xW_{1-x}S_2$ alloys, and WS_2−MoS_2 heterostructures without any modifications to the growth hardware. Compared with alkali metal-assisted MOCVD,[29−32] Hy-MOCVD not only yields similar benefits of increased grain size and suppressed multilayer nucleation but also provides an effective strategy for engineering the growth promoter concentration, transition metal dopants, alloy composition, and heterostructures of TMDCs on versatile substrates for a wide range of academic research.

RESULTS AND DISCUSSION

In Figure 1, we compare the concepts and strengths of SS-CVD, MOCVD, and Hy-MOCVD. The Hy-MOCVD method employs both X-organic precursors used in MOCVD and inorganic transition metal precursors (M-inorganic) used in SS-CVD. As in MOCVD, the X-organic precursor was introduced into the Hy-MOCVD chamber in the vapor phase via a bubbler and a mass flow controller (see Figure

https://doi.org/10.1021/acsnano.4c02164
ACS Nano 2024, 18, 25414−25424

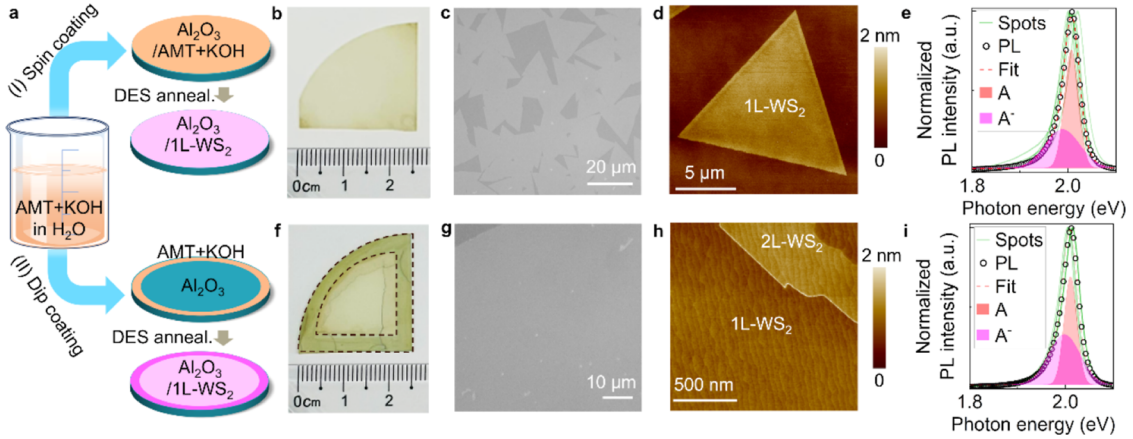

Figure 2. Hy-MOCVD processes. (a) Schematics of the two paths to Hy-MOCVD: (I) spin-coating and (II) dip-coating. (b–e) Characterization of representative WS_2 film synthesized via spin-coating (Path I), consisting of (b) photograph of *c*-plane sapphire/WS_2 wafer, (c) contrast-enhanced optical microscope image, (d) AFM topography image, and (e) normalized photoluminescence (PL) spectra collected from 8 random spots on spin-coating Hy-MOCVD monolayer WS_2, including overlaid Gaussian peaks fit to the narrowest spectrum. (f–i) Characterization of representative WS_2 synthesized via dip-coating (Path II), consisting of: (f) photograph, (g) optical micrograph, (h) AFM topography image, and (i) normalized PL spectra collected from 8 random spots, with overlaid fit to narrowest spectrum. Overlaid dashed lines in (f) highlight the dip-coated area on the edges of *c*-plane sapphire wafer.

S1 for the setup schematic of Hy-MOCVD). This ensures a stable chalcogen concentration throughout the entire growth process, which is necessary for stoichiometrically controlled growth. Precise combinations of the primary transition metal element(s), substitutional dopants, and any growth promoter species are more challenging to deliver due to their lower vapor pressure, yet these are also critical to the outcome of the growth process.[23,26] To overcome the uncontrolled flux of SS powders and the expense of metal–organic precursor delivery, M-inorganic precursors with growth promoter KOH were deposited onto the growth substrate by aqueous solution coating before Hy-MOCVD growth. This localized transition metal supply ensures a high concentration of reactive M species on the wafer surface during growth. Moreover, by mixing M-inorganic and KOH with other dopant sources,[8,9,35,36] Hy-MOCVD can be used for the growth of doped TMDCs and TMDC alloys with extreme precision via dilution.[12,36] Summarizing these advantages (Table S1), Hy-MOCVD combines the precise control over chalcogen stoichiometry found in MOCVD with the versatility and efficiency in switching or mixing transition metals and growth promoters offered by SS-CVD. In the following sections, we will demonstrate these advantages by using Hy-MOCVD to grow WS_2 and incorporate dopants, alloys, and heterostructures.

In the Hy-MOCVD growth of WS_2, diethyl sulfide (DES, $(CH_3CH_2)_2S$) and ammonium metatungstate hydrate (AMT, $(NH_4)_6H_2W_{12}O_{40}{\cdot}xH_2O$) were used as the X-organic and M-inorganic precursors, respectively. Delivery of the metal solution to the substrate is flexible, and we explored two paths in this work: spin- and dip-coating (Figure 2a). In spin-coating delivery, the starting solution of AMT and KOH in deionized (DI) water was spin coated onto a UV–ozone-treated wafer, and the water was removed by heating at 80 °C in air. The coated wafer was then transferred to the tube furnace MOCVD system and annealed in a DES vapor environment (0.05–0.12 sccm) at 775 °C for 2–6 h to conduct the growth. Photographs of a typical WS_2 on *c*-plane sapphire wafer after the growth show a uniform color across the wafer (Figure 2b). Optical microscopy images show homogeneous coverage of WS_2 triangular domains, typically ~20 μm in width, with sharp and straight edges (Figure 2c). Atomic force microscopy (AFM) shows the monolayer thickness and clean surface of Hy-MOCVD grown WS_2 (Figures 2d and S2). Typical photoluminescence (PL) spectra show strong and narrow neutral exciton peaks (A) at 2.01 eV with the narrowest full width at half-maximum (fwhm) of 28 meV (Figures 2e and S3), indicating the good quality of Hy-MOCVD grown WS_2.[37,38] The lower-energy shoulder peak is attributed to the negatively charged exciton (A^-), consistent with the n-type electronic transport characteristics observed in Hy-MOCVD WS_2 monolayers, as discussed in a later section.

In dip-coating delivery, the *c*-plane sapphire wafer edges were dipped into an aqueous solution of AMT and KOH. As with the spin-coating path, the dip-coated wafer was then dried in air at 80 °C, and annealed in DES. During the growth process, reactive species diffuse from the highly concentrated AMT + KOH sources at the sample edges, triggering the growth of WS_2 on the uncoated center area of the wafer. Typical photos of the wafer show deeper color on the dip-coated edges and uniform light yellow-green in the center of the wafer (Figure 2f). An optical micrograph taken from the center of the wafer shows a continuous WS_2 film with small multilayer islands (Figure 2g). AFM images acquired around a multilayer island show well-defined single-layer-height steps of the bilayer island and clear atomic steps and terraces of the *c*-plane sapphire substrate visible through the monolayer, indicating the clean surface of the WS_2 film (Figure 2h). PL spectra collected from continuous monolayer regions of these samples typically show A exciton peaks centered at 2.01 eV (with the narrowest fwhm of 27 meV), consistent with a good-quality monolayer film (Figures 2i and S3).[37] We have found that both spin-coating and dip-coating yield good-quality and consistent growth. Using X-ray photoelectron spectroscopy (XPS), we detected trace signatures for residual K following Hy-MOCVD growth on WS_2 samples grown using both spin-coating and dip-coating precursor delivery. We observe that this signal is removed during wet transfer processes (Figure S4a), which suggests that the residual K species are not incorporated within the WS_2 lattice. Dip-coating Hy-MOCVD

https://doi.org/10.1021/acsnano.4c02164
ACS Nano 2024, 18, 25414–25424

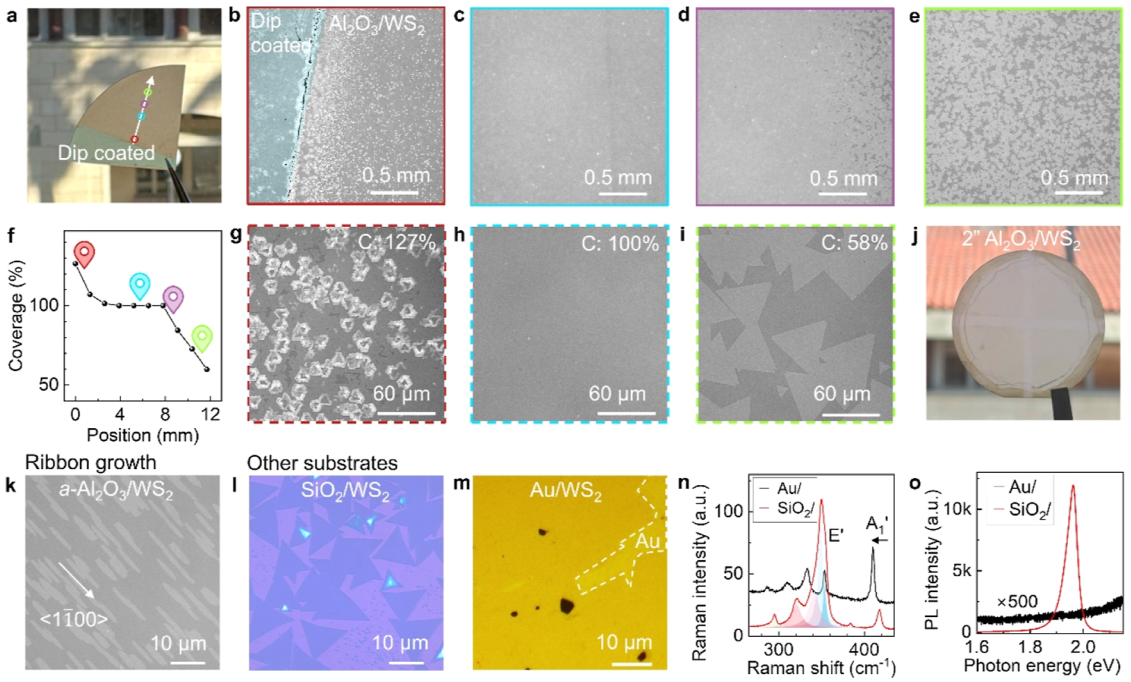

Figure 3. Morphology control and compatibility with other substrates. (a) Photo of Hy-MOCVD grown *c*-plane sapphire/WS_2 wafer, with a single edge dip-coated by precursor solution. (b−e) Contrast-enhanced optical images of sapphire/WS_2 taken from the locations highlighted by colored circles in (a). (f) WS_2 coverage versus position along the arrow in (a). Positions of (b−e) are highlighted with corresponding colors. (g−i) Contrast-enhanced zoom-in optical images of multilayer, continuous monolayer, and noncontinuous monolayer regions. *C* stands for the coverage extracted from the corresponding image. (j) Photo of Hy-MOCVD grown WS_2 on a 2″ *c*-plane sapphire wafer via dip-coating. (k) Optical image of Hy-MOCVD grown WS_2 ribbons on annealed *a*-plane sapphire with 1° miscut angle toward *c*-plane. (l) Optical image of Hy-MOCVD WS_2 grown on Si/SiO_2 substrate. (m) Optical image of Hy-MOCVD grown WS_2 grown on sapphire/Au substrate. (n,o) Raman and PL spectra of WS_2 grown on SiO_2 and Au substrates, respectively.

can grow continuous monolayer WS_2 on sapphire on demand over a long period up to 17 months, showcasing the excellent repeatability of Hy-MOCVD (Figure S5). To demonstrate that Hy-MOCVD can be broadly applied to other TMDCs, we grew monolayer MoS_2 and WSe_2 with dip-coating Hy-MOCVD (Figure S6).

Growth producing a well-defined compositional gradient can be valuable for exploratory synthesis. Dip-coating Hy-MOCVD can exploit the vapor-phase transport gradient to grow WS_2 with different morphologies and high compatibility with different substrates. Figure 3a shows a photograph of the *c*-plane sapphire wafer after Hy-MOCVD growth with only one edge coated with AMT + KOH solution. The WS_2 coverage changes with increasing distance from the dip-coating boundary (Figure 3b−e), with a typical profile given by Figure 3f (extracted from binary thresholding of microscope images; coverage over 100% indicates multilayer islands over a continuous monolayer film). At higher magnification within these regions, we observed that WS_2 grew as a continuous film with a high density of multilayer islands in the area close to the dip-coating boundary (Figure 3g). This converts to a continuous monolayer with a low density of multilayer islands in the center of the wafer (Figure 3h) and finally becomes isolated domains on the far end (Figure 3i). The high coverage region (>70%) of predominantly monolayer WS_2 extends to approximately 1 cm away from the dip-coating metal source region, which is typical of samples grown in this way. Ozone etching reveals the grain boundaries[39] within the continuous WS_2 regions (Figure S7), and we observe that the average WS_2 domain size varies from 3 to 30 μm with increasing distance from the dip-coating boundary.

As shown in Figure 3j, dip-coating can be applied to enable Hy-MOCVD growth across a 2″ *c*-plane sapphire wafer. The coverage and uniformity near the wafer center were improved by dip-coating the wafer edge and placing two crossed AMT + KOH dip-coated W foil strips on the substrate. This setup increases the local flux of W-species near the wafer center. The uniformity of Hy-MOCVD growth across the 2″ sapphire wafer was evaluated by Raman mapping (Figure S8), which demonstrated that the WS_2 film grown on the bare sapphire area is primarily monolayer, with an average 2LA + E′ to A_1' peak distance of 65.4 ± 0.8 cm^{-1}, and exhibits a crystalline quality similar to SS-CVD, with an average A_1' peak width of 5.0 ± 0.5 cm^{-1}.[6,40] The narrow distributions of both metrics confirm the uniformity of Hy-MOCVD WS_2.

Growth on multiple substrates is important for the laboratory-scale optimization and integration of TMDCs. Hy-MOCVD growth of WS_2 on annealed *a*-plane sapphire substrates with 1° miscut angle toward the *c*-plane (Figure 3k) resulted in WS_2 ribbons oriented along the substrate ⟨1$\bar{1}$00⟩ terrace edge direction (see Figure S9 for the AFM images). This morphology is consistent with previous observations of epitaxial growth of MoS_2 and WS_2 on *a*-plane and vicinal *a*-plane sapphire via SS-CVD,[7,41] which is attributed to the anisotropic growth induced by the 2-fold symmetry *a*-plane sapphire lattice. Polarization-resolved second-harmonic generation (SHG) reveals that the Hy-MOCVD grown WS_2 ribbons exhibit predominantly two sets of epitaxial lattice orientations, with the WS_2 armchair directions oriented parallel to either the ⟨1−100⟩ or ⟨0001⟩ directions of the *a*-plane sapphire (Figure S10). However, this epitaxial behavior is different from the unidirectional epitaxial

https://doi.org/10.1021/acsnano.4c02164
ACS Nano 2024, 18, 25414−25424

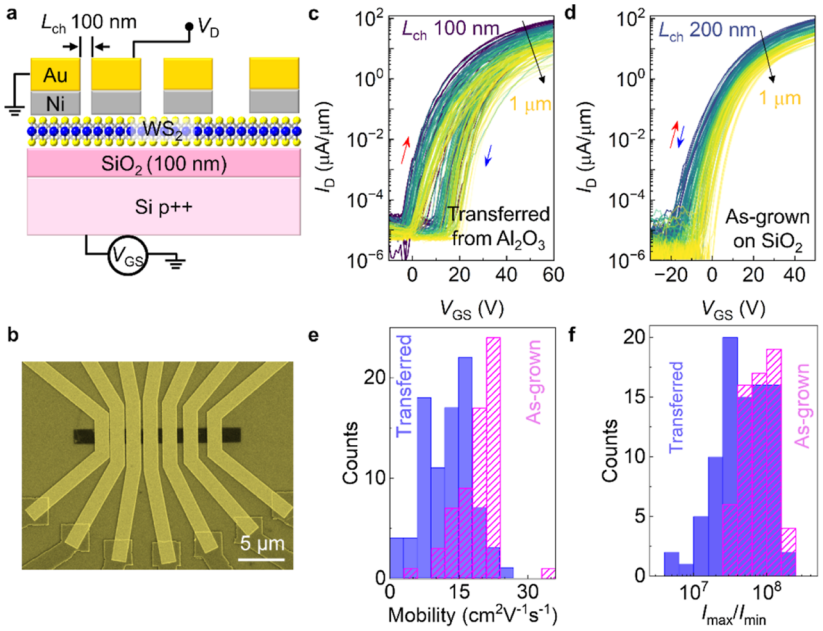

Figure 4. Electrical characteristics of monolayer WS_2 grown by Hy-MOCVD. (a) Schematic of a back-gated transistor based on Hy-MOCVD WS_2. (b) False color SEM image of WS_2-based TLM device. (c) Measured I_D vs V_{GS} curves for FETs of transferred Hy-MOCVD WS_2 with designed channel length L_{ch} of 100, 200, 300, 500, 700, and 1000 nm, from purple to yellow at V_{DS} = 1 V. Red and blue arrows represent the forward and backward V_{GS} sweeping directions, respectively. (d) Measured I_D vs V_{GS} curves for FETs of as-grown Hy-MOCVD WS_2 with designed channel length L_{ch} of 200, 300, 500, 700, and 1000 nm (from blue to yellow). Red and blue arrows represent the forward and backward V_{GS} sweeping directions, respectively. Histograms of measured (e) field-effect mobility and (f) I_{max}/I_{min} for FETs of transferred and as-grown Hy-MOCVD WS_2 (extracted from forward V_{GS} sweeps).

growth of MoS_2 and WS_2 on *a*-plane sapphire and vicinal *a*-plane sapphire, which can be attributed to the difference between the substrate miscut angle, substrate annealing conditions, and growth chemistry. Previous studies have reported that the use of alkali metal salts can have an impact on epitaxial behavior as well.[32] Our results suggest that Hy-MOCVD can realize van der Waals epitaxial growth of 2D TMDCs and can be used for understanding how precursors and alkali metal-based growth promoters modify epitaxy. Additionally, Hy-MOCVD is compatible with the growth of WS_2 on standard thermally oxidized Si/SiO_2 substrates and on Au thin films deposited on *c*-plane sapphire substrates (Figure 3l,m). Notably, the Raman out-of-plane mode (A_1') of WS_2 on Au exhibits a redshift of ~7 cm^{-1}, shifting the peak center to 410 cm^{-1}, while the in-plane mode (E') remains unaltered at ~354 cm^{-1} compared to WS_2 grown on SiO_2 (Figure 3n). This observation aligns with the reported A_1' mode downshifting in exfoliated WS_2 monolayer on Au and suggests a strong interaction between monolayer WS_2 and Au.[42] PL of WS_2 grown on Si/SiO_2 confirms its high quality, whereas the quenched PL for WS_2 grown on Au indicates nonradiative transition dominated recombination of excitons in the Au/WS_2 stack (Figure 3o). Furthermore, Hy-MOCVD WS_2 on different substrates exhibited an absence of Raman peaks within the 1300−1600 cm^{-1} range (see Figure S11 for the Raman spectra), indicating that the films are free of amorphous carbon. Figure S4b presents a comparison between C 1s core-level spectra for Hy-MOCVD WS_2 and those of the bare substrate, which confirms the absence of carbon deposition during the growth process.

To evaluate the electronic properties of Hy-MOCVD grown WS_2, we fabricated back-gated field-effect transistors (FETs) through two processes: by transferring the Hy-MOCVD monolayer WS_2 from sapphire onto SiO_2 (100 nm) on highly doped p^{++} Si and by using as-grown Hy-MOCVD monolayer WS_2 directly on similar substrates. FET channel regions (100 nm to 1 μm) were defined by electron-beam lithography on WS_2 triangular domains and contacted with Ni/Au electrodes to achieve transfer length method (TLM) structures (Figure 4a,b).[43] Measured drain current vs back-gate voltage (I_D vs V_{GS}) characteristics of such WS_2 FETs exhibit consistent n-type behavior across 10−17 devices for each channel length, illustrating the uniformity of Hy-MOCVD grown WS_2 (Figure 4c,d).

The devices with transferred WS_2 exhibit maximum electron mobility between 24 and 33 $cm^2\ V^{-1}\ s^{-1}$ (this value is given as a range of two numbers, extracted from the forward and backward sweeps, due to the observed clockwise hysteresis), with an average value between 13 and 18 $cm^2\ V^{-1}\ s^{-1}$ and median value between 13 and 19 $cm^2\ V^{-1}\ s^{-1}$. We see a notable average I_{max}/I_{min} ratio of 10^7 (Figure 4e,f). The shortest devices with a 100 nm channel length have a good on-state current density, reaching a maximum value of 88 $\mu A/\mu m$ and an average of 65 $\mu A/\mu m$ at V_{DS} = 1 V (see Figure S12a for the I_D versus channel length plot). These metrics surpass those of most SS-CVD and MOCVD-grown monolayer WS_2-based FETs with similar configurations, indicating the good quality of Hy-MOCVD WS_2 (Table S3 for a device performance comparison). The contact resistance can lead to errors in the field-effect mobility estimate, especially in shorter channel length devices (Figure S12c shows field-effect mobility versus channel length). The device performance can potentially be improved by incorporating lower resistance contacts and high-κ dielectric layers.[44−47] FET devices fabricated from Hy-MOCVD WS_2 grown directly on the Si/SiO_2 substrate exhibit improved field-effect mobility with a maximum between 34

https://doi.org/10.1021/acsnano.4c02164
ACS Nano 2024, 18, 25414−25424

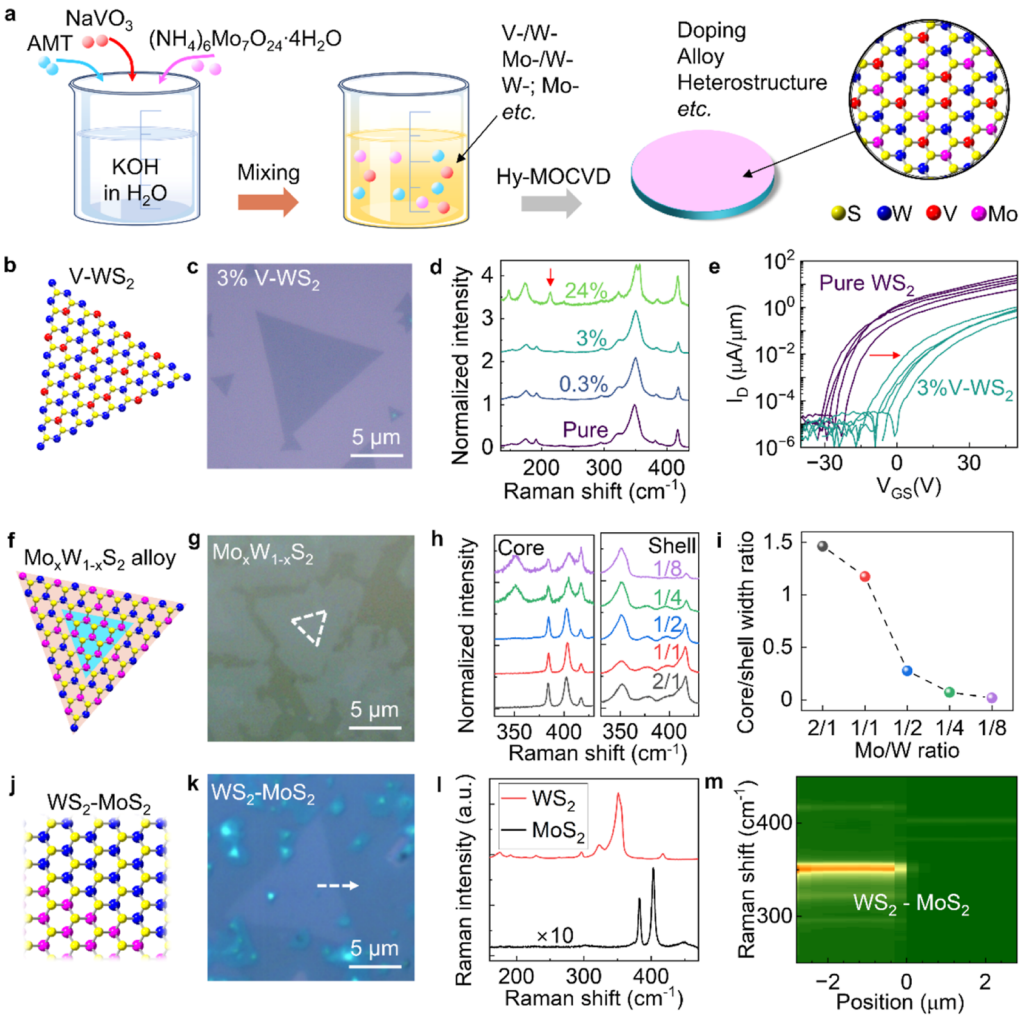

Figure 5. Transition metal engineering of monolayer WS_2 using Hy-MOCVD. (a) Schematic of transition metal engineering of monolayer WS_2 using Hy-MOCVD. (b) Lattice schematic of V-doped WS_2. (c) Optical image of as-grown Hy-MOCVD V-doped WS_2 on Si/SiO_2 substrate with a nominal doping concentration of 3%. (d) Typical Raman spectra of V-doped WS_2 with different nominal doping ratios of 0, 0.3, 3, and 24%. (e) Measured I_D vs V_{GS} curves for monolayer undoped WS_2 and V-doped WS_2 FET devices with channel length of 500 nm and V_{DS} = 1 V. (f) Lattice schematic of in-plane MoS_2−$Mo_xW_{1-x}S_2$ heterostructure with a MoS_2 core and a $Mo_xW_{1-x}S_2$ alloy shell. (g) Optical image of Hy-MOCVD grown in-plane MoS_2−$Mo_xW_{1-x}S_2$ heterostructure on *c*-plane sapphire substrate. MoS_2 core is circled with a white dashed line. (h) Typical Raman spectra of $Mo_xW_{1-x}S_2$ alloy core (left) and shell (right) grown with different Mo/W mole ratios in the starting solution of Hy-MOCVD. (i) Core/shell width ratio versus Mo/W mole ratio of starting solution. (j) Lattice schematic of Hy-MOCVD grown WS_2−MoS_2 in-plane heterostructure. (k) Optical image of Hy-MOCVD grown WS_2−MoS_2 in-plane heterostructure. (l) Typical Raman spectra collected from the two sides of WS_2−MoS_2 in-plane heterostructure. (m) Raman spectra line scan along the arrow in (k).

and 36 $cm^2\ V^{-1}\ s^{-1}$, an average value of 19−21 $cm^2\ V^{-1}\ s^{-1}$, a median value of 20−22 $cm^2\ V^{-1}\ s^{-1}$ (Figure 4e), and less I_D hysteresis for forward-to-backward V_{DS} sweeps (Figures 4c,d and S12c−h). This suggests that the performance of Hy-MOCVD grown on sapphire substrates is limited by either transfer-induced damage (see broadened Raman and PL peaks of WS_2 after the transfer in Figure S13) or a difference in crystal quality versus growth on Si/SiO_2 substrates.

Directly incorporating dopants into TMDCs and growing TMDC alloys and heterostructures from synthesis have sparked substantial interest. Hy-MOCVD enables convenient adjustment of the TMDC metal composition based on the precise addition of various water−soluble transition metal sources to the precursor solution (Figure 5a). V-doped WS_2 monolayers with a nominal doping from 0.3 to 24% (V/(V + W) atom mole ratio in the precursor solution) were grown on Si/SiO_2 substrates (Figure 5b,c) by adding sodium metavanadate ($NaVO_3$) into the AMT + KOH precursor solution. The emergence of a Raman mode at around 213 cm^{-1} in nominal 24% V-doped WS_2, and the decrease of the 2LA(M) + E′ peak intensity with the increase of the nominal doping ratio, are consistent with previous V-WS_2 literature (see Figures 5d and S14 for nominal doping ratio dependence of 2LA + E′ peak intensity).[9,48] The characteristic peak at 213 cm^{-1} can be assigned to the multiphonon mode of E″(M)−TA(M), suggesting that V is substitutionally incorporated into WS_2.[48] Transistors fabricated using the 3% V-doped WS_2 exhibit a threshold voltage shift of +23 V compared with undoped WS_2 devices (Figure 5e), on the 100 nm SiO_2 back-gate insulators. This is consistent with the expected p-type doping from substitutional V acceptors in the TMDC monolayer.[9,36] Additional optimizations of doping concentration and FET metal contacts are needed to achieve a hole current. XPS characterization (Figure S15) shows the measured V/(V + W)

https://doi.org/10.1021/acsnano.4c02164
ACS Nano 2024, 18, 25414−25424

atom ratio increasing monotonically with nominal doping concentration, accompanied by shifting of the W 4f and S 2p core levels toward lower binding energy as expected for a p-type dopant. We also demonstrated Re doping in Hy-MOCVD. Compared with pure WS_2, we found that the PL emission is evidently quenched in both V-doped and Re-doped WS_2 (Figure S16). These observations are consistent with previous reports of quenched PL in doped samples, including V-WS_2, Re-WSe_2, V-MoS_2, and Re-MoS_2,[9,11,49] where the PL quenching can be attributed to the in-gap dopant state-mediated exciton recombination and/or additional charge carriers.[12,49]

Hy-MOCVD similarly enables alloy and heterostructure growth. We grew $Mo_xW_{1-x}S_2$ alloys exhibiting an in-plane heterostructure with a core and a shell of different alloy compositions during a single-step dip-coating Hy-MOCVD growth (Figure 5f,g) by mixing ammonium molybdate ($(NH_4)_6Mo_7O_2{\cdot}4H_2O$) into the AMT + KOH solution. We provide additional confirmation of the core−shell compositional variation via fluorescence imaging of the MoS_2 and WS_2 PL emission on a transferred alloy sample in Figure S17a,b and XPS characterization, which shows the coexistence and splitting of the Mo and W elemental electron core energy levels in the alloy core−shell sample (Figure S17c,d). The Mo/W molar ratio of the precursor solution influenced the $Mo_xW_{1-x}S_2$ alloy core−shell dimension and alloy compositions, as illustrated in Figure 5h,i. For example, a 2:1 Mo/W ratio yielded a MoS_2 core with a WS_2-like alloy shell (i.e., an alloy closer in Raman signature to the signature of pure WS_2), whereas the decrease to a 1:8 Mo/W ratio resulted in a MoS_2-like core with a WS_2 shell. The core−shell structure evidently results from differences in vapor-phase or on-surface transport kinetics for the W and Mo precursors.[50,51]

In contrast, two sequential Hy-MOCVD growths of W followed by Mo precursors resulted in WS_2−MoS_2 in-plane heterostructures (Figure 5j,k). Raman spectra collected from two sides of the WS_2−MoS_2 heterostructure show distinct MoS_2 and WS_2 peaks without significant alloying (Figure 5l), and a Raman spectrum line scan shows a distinct interface between WS_2 and MoS_2 (Figure 5m). Multilayer MoS_2 nucleation also occurred on top of WS_2 and at the interface of the heterostructure. This shows the capabilities of Hy-MOCVD for growing WS_2−MoS_2 heterostructures with different layer numbers and vertical stacking.

CONCLUSIONS

In summary, we have demonstrated that Hy-MOCVD provides an effective strategy for rapidly synthesizing TMDC monolayers with diverse transition metal dopants, alloy elements, and heterostructures, offering a versatile platform for exploring synthesis to realize enhanced and tailored electronic, optical, and magnetic properties in TMDC monolayers and heterostructures.

EXPERIMENTAL METHODS

Material Growth and Transfer. Hy-MOCVD commenced with the preparation of an initial aqueous solution comprising transition metal precursors and promoters. In the case of pure WS_2 growth, 0.6 g of AMT and 0.05−0.1 g of KOH were dissolved in 30 mL of DI water. For V-doped WS_2 growth, around 90 mg of $NaVO_3$ was introduced into the 30 mL AMT + KOH solution to achieve 24% V/(V + W) atom mole ratio in the solution. Ultrasonication was employed to facilitate the dissolution of $NaVO_3$. $NaVO_3$ was not fully dissolved, and the cloudy solution was used for growing a 24% V-WS_2 sample. The cloudy solution was diluted multiple times to get 3 and 0.3% V/(V + W) atom mole ratio solutions. In these low V/(V + W) ratio solutions, $NaVO_3$ appeared to be fully dissolved. For Re-doped WS_2 growth, NH_4ReO_4 was used as a Re source. For $Mo_xW_{1-x}S_2$ alloy growth, AMT + KOH (0.6 g + 0.05 g in 30 mL DI water) and ammonium molybdate + KOH (0.43 + 0.2 g in 30 mL DI water) solutions were made separately and mixed with different volume ratios from 2/1 to 1/8. For the growth of WS_2−MoS_2 heterostructures, two-step dip-coating Hy-MOCVD was used to grow WS_2 and MoS_2 sequentially. In the dip-coating path of Hy-MOCVD, the aqueous solution was dip-coated onto one or all edges of ozone-treated sapphire substrates, followed by N_2 blow drying. For the dip-coating Hy-MOCVD growth on a 2 inch *c*-plane sapphire wafer, in addition to coating the wafer edge, two initial solution coated W foil strips were placed on the top of the wafer, forming a cross and sitting at its center. In the spin-coating path of Hy-MOCVD, 0.25 mL of 10−16 times diluted initial solution was spin-coated onto ozone-treated sapphire and Si/SiO_2 substrates at 1000 rpm for 1 min. When growing on Si/SiO_2 and sapphire/Au, no ozone was applied before dip-coating. For the growth of WS_2 on *a*-plane sapphire (Hefei Crystal Technical Material Co., Ltd., *a*-plane off *c*-plane 1.0 ± 0.1°), the wafer was annealed in a muffle furnace at 1200 °C for 12 h in an ambient air environment. The *c*-plane sapphire wafers (Valley Design Corp., 28362-1) used in this paper were not annealed. The solution-coated substrates were baked on a hot plate at 80 °C for 1 min and quickly loaded into a MOCVD tube furnace. The tube was evacuated to <0.5 Torr and filled with a flowing mixture of 1600 sccm Ar and 10 sccm H_2. The furnace temperature was ramped to 725−775 °C over 30 min. Changes to the growth temperature will modify the active concentration of the transition metal and growth promoter species on the substrate surface, and therefore, the composition of the precursor solution may need to be separately optimized for large changes in growth temperature. Subsequently, the H_2 flow was adjusted to 1 sccm, and 0.05−0.12 sccm of DES was introduced into the tube furnace. The substrates underwent annealing in this environment for 2−6 h to complete growth. Postgrowth, the DES flow was reduced to 0.025−0.1 sccm, and the furnace heating was discontinued. DES flow was closed when the furnace naturally cooled to 300 °C, and substrates were unloaded at room temperature.

WS_2 grown on sapphire substrates was transferred onto Si/SiO_2 substrates using a poly(methyl methacrylate) (PMMA)-assisted transfer method. The samples were spin-coated with PMMA and dried on a hot plate at 100 °C for 3 min. WS_2/PMMA was delaminated from the sapphire substrate by gradually dipping the substrate into DI water (the substrate was in an upward-facing position and angled at 30−60° relative to the water surface) and transferred onto the target substrate with SiO_2 (100 nm) on Si, followed by drying on a hot plate at 100 °C for 5 min. The PMMA layer was removed by soaking it in acetone at 60 °C for 15 min.

Device Fabrication and Analysis. For the transferred devices shown in Figure 4c, monolayer WS_2 was grown on sapphire with dip-coating Hy-MOCVD and transferred off by using a PMMA-based transfer (as described above) onto 100 nm SiO_2 on Si. For the devices fabricated on the Si/SiO_2 growth substrate, shown in Figure 4d, dip-coating Hy-MOCVD monolayer WS_2 was directly grown on SiO_2 (100 nm) on p^{++} Si (≤0.005 Ω·cm) that also served as the back-gate. Alignment marks were first patterned on the direct-grown sample, such that discrete WS_2 crystals could be identified. Devices were made on single crystalline WS_2 triangles to avoid the existence of grain boundaries in the device channels. The measured devices were sampled randomly from within a 5 × 5 mm^2 region on each chip. Electron-beam lithography was employed for each lithography step. Large probing pads (SiO_2/Ti/Pt 10/2/20 nm) were first patterned and deposited by electron-beam evaporation via lift-off. SiO_2 was used in the probing pad to limit the pad-to-substrate leakage. XeF_2 was used for channel definition, and the contact region was patterned for lift-off. 15/30 nm Ni/Au contacts were electron-beam evaporated at ~10^{-8} Torr, and a rate of 0.5 Å/s. 20/35 nm Ni/Au contacts were deposited for the nontransferred devices. The fabricated transistors

https://doi.org/10.1021/acsnano.4c02164
ACS Nano 2024, 18, 25414−25424

were measured in a Janis ST-100 probe station at ~10^{-4} Torr under vacuum using a Keithley 4200 semiconductor parameter analyzer.

For the undoped and the V-doped WS_2 devices shown in Figure 5e, the starting WS_2 and V-WS_2 were grown on 100 nm SiO_2 on Si with spin-coating Hy-MOCVD. Alignment marks were patterned to identify monolayer regions on both samples. Metal pads and channels were defined by e-beam lithography, as described above. For both the doped and undoped WS_2, Ru/Au (5/50 nm) were deposited via e-beam evaporation to investigate potential p-type transport from V-doped WS_2, based on previous reports of good p-type performance from Ru contacts.[42] The devices were measured under vacuum as described above.

Threshold voltage was extracted at a constant current of 10 nA/μm.[52] The field-effect mobility $\mu_e = \max(g_m)/[C_{ox}V_{DS}(W_{ch}/L_{ch})]$, was estimated using the maximum transconductance of forward and backward V_{GS} sweeps, $g_m = dI_D/dV_{GS}$, and the gate insulator capacitance per unit area is $C_{ox} = \varepsilon_0\kappa_{ox}/t_{ox}$. The SiO_2 gate oxide thickness t_{ox} = 100 nm, the oxide relative permittivity κ_{ox} = 3.9, ε_0 is the vacuum permittivity, and V_{DS} = 1 V. W_{ch} and L_{ch} are channel width and length, respectively. The designed W_{ch} was 2.0 μm. The final W_{ch} was measured via SEM to be 1.6 μm for FETs of transferred WS_2 and 2.0 μm for FETs of as-grown WS_2. The final L_{ch} in the FETs of transferred WS_2 were measured via SEM to be 72, 175, 261, 461, 650, and 973 nm, corresponding to the designed L_{ch} values of 100, 200, 300, 500, 700, and 1000 nm, respectively. The final L_{ch} in the FETs of as-grown WS_2 were measured via SEM to be 173, 275, 477, 681, and 993, corresponding to the designed L_{ch} values of 200, 300, 500, 700, and 1000 nm, respectively. The mobilities of the FETs were corrected with these measured W_{ch} and L_{ch} values.

Material Characterizations. AFM imaging was conducted utilizing a Bruker ICON AFM using the ScanAsyst topography imaging mode with a NSC19/Al-BS tip. Raman and PL spectra were acquired at room temperature with 532 nm laser excitation using a HORIBA Scientific LabRAM HR Evolution confocal microscope. Optical microscope imaging was performed using an Olympus BX-51 microscope in epi-reflection geometry. The optical microscope contrast for images in Figures 2c,g and 3b−e,g−i,k were enhanced in the following way: after acquisition, we converted the color images to grayscale and increased the contrast and brightness to improve visibility of the WS_2 on the transparent sapphire wafer. SHG was performed using a femtosecond laser (NKT Origami Onefive 10, 1030 nm, <200 fs) at room temperature. A 40× objective lens was used to excite the sample with an average power of 5−10 mW, and the signal was collected in reflective geometry by an EMCCD (Andor iXon Ultra) with an integration time of 100 ms at each polarization angle. XPS was performed using PHI VersaProbe 3.

ASSOCIATED CONTENT

Supporting Information

The Supporting Information is available free of charge at https://pubs.acs.org/doi/10.1021/acsnano.4c02164.

Schematic of Hy-MOCVD setup, high magnification AFM of spin-coating grown WS_2, PL peak fitting results, XPS of potassium and carbon element, growth results over 17 months, optical images and Raman of MoS_2 and WSe_2, continuous WS_2 monolayer domain size extraction, AFM of WS_2 grown on *a*-plane sapphire, SHG characterizations of WS_2 ribbons grown on *a*-plane sapphire, wide range Raman spectra of WS_2 grown on sapphire and SiO_2, L_{ch} vs I_D, mobility, hysteresis, and typical I_D vs V_{GS} hysteresis, PL, and Raman comparison between as-grown and transferred WS_2, and Raman 2LA + E′ peak intensity vs nominal doping concentration of V-doped WS_2, XPS of V-doped WS_2, PL of V-doped and Re-doped WS_2, XPS of alloy, tables of the comparison of growth metric, MOCVD growth parameters, and FET performance (PDF)

AUTHOR INFORMATION

Corresponding Author

Andrew J. Mannix − *Department of Materials Science & Engineering, Stanford University, Stanford, California 94305, United States; Stanford Institute for Materials and Energy Sciences, SLAC National Accelerator Laboratory, Menlo Park, California 94025, United States;* orcid.org/0000-0003-4788-1506; Email: ajmannix@stanford.edu

Authors

Zhepeng Zhang − *Department of Materials Science & Engineering, Stanford University, Stanford, California 94305, United States;* orcid.org/0000-0002-9870-0720

Lauren Hoang − *Department of Electrical Engineering, Stanford University, Stanford, California 94305, United States;* orcid.org/0009-0001-7556-8560

Marisa Hocking − *Department of Materials Science & Engineering, Stanford University, Stanford, California 94305, United States;* orcid.org/0000-0002-5884-7832

Zhenghan Peng − *Department of Materials Science & Engineering, Stanford University, Stanford, California 94305, United States*

Jenny Hu − *Department of Applied Physics, Stanford University, Stanford, California 94305, United States;* orcid.org/0000-0002-7775-4391

Gregory Zaborski, Jr. − *Department of Materials Science & Engineering, Stanford University, Stanford, California 94305, United States*

Pooja D. Reddy − *Department of Materials Science & Engineering, Stanford University, Stanford, California 94305, United States*

Johnny Dollard − *Department of Materials Science & Engineering, Stanford University, Stanford, California 94305, United States*

David Goldhaber-Gordon − *Department of Physics, Stanford University, Stanford, California 94305, United States; Stanford Institute for Materials and Energy Sciences, SLAC National Accelerator Laboratory, Menlo Park, California 94025, United States*

Tony F. Heinz − *Department of Applied Physics and Department of Photon Sciences, Stanford University, Stanford, California 94305, United States; Stanford Institute for Materials and Energy Sciences, SLAC National Accelerator Laboratory, Menlo Park, California 94025, United States*

Eric Pop − *Department of Materials Science & Engineering, Stanford University, Stanford, California 94305, United States; Department of Electrical Engineering and Precourt Institute for Energy, Stanford University, Stanford, California 94305, United States;* orcid.org/0000-0003-0436-8534

Complete contact information is available at: https://pubs.acs.org/10.1021/acsnano.4c02164

Author Contributions

[▽]Z.Z. and L.H. contributed equally to this work. Z.Z. and L.H. developed the growth recipe under the supervision of A.J.M. and E.P. Z.Z. performed the material growth and characterizations. L.H. fabricated the devices and conducted the device measurements and analysis under the supervision of A.J.M. and E.P. M.H. developed the sapphire annealing recipe with J.D. under the supervision of A.J.M. M.H. performed SHG measurements with the help of J.H. under the supervision of T.F.H. Z.P. performed the XPS measurements. P.R. and G.Z.,

https://doi.org/10.1021/acsnano.4c02164
ACS Nano 2024, 18, 25414−25424

Jr. built the MOCVD system under the supervision of A.J.M. Z.Z. and A.J.M. wrote the paper with input from L.H. All authors participated in discussions, reviewed, and approved the manuscript.

Notes

The authors declare no competing financial interest.

ACKNOWLEDGMENTS

This work was primarily supported by the U.S. Department of Energy (DOE), Office of Science, Office of Basic Energy Sciences, Division of Materials Sciences and Engineering under award DE-SC0021984 (Stanford University: Z.Z., M.H., A.J.M.) for the development of the Hy-MOCVD process, thin film and heterostructure growth, and optical microscopy and AFM characterization, and FWP 100740 (SLAC National Accelerator Laboratory: T.F.H., D.G.-G.) for SHG measurements and for PL and Raman spectroscopy. XPS measurements were supported under FWP 10029 (Z.P.). Additional funding for the fabrication and measurement of transistors was provided by the SUPREME Center, jointly sponsored by the SRC and DARPA, and from TSMC under the Stanford SystemX Alliance (L.H. and E.P.), and from the Precourt Institute for Energy at Stanford University. This work was completed in part at the Stanford Nano Shared Facilities (SNF), supported by the National Science Foundation under award ECCS-2026822, and at the nano@Stanford laboratories, supported by the National Science Foundation as part of the National Nanotechnology Coordinated Infrastructure award ECCS-1542152. M.H. acknowledges partial support from the Department of Defense through the Graduate Fellowship in STEM Diversity program. J.H. acknowledges partial support from an NTT Graduate Research Fellowship. G.Z., Jr. and P.R. acknowledge support from the National Science Foundation Graduate Research Fellowship and Stanford Graduate Fellowship in Science and Engineering. The authors thank A.-T. Hoang, X. Zhu, and K. Mukherjee for the helpful discussions and comments on the manuscript.

REFERENCES

(1) Xia, F.; Wang, H.; Xiao, D.; Dubey, M.; Ramasubramaniam, A. Two-Dimensional Material Nanophotonics. *Nat. Photonics* **2014**, *8*, 899−907.

(2) O'Brien, K. P.; Naylor, C. H.; Dorow, C.; Maxey, K.; Penumatcha, A. V.; Vyatskikh, A.; Zhong, T.; Kitamura, A.; Lee, S.; Rogan, C.; Mortelmans, W.; Kavrik, M. S.; Steinhardt, R.; Buragohain, P.; Dutta, S.; Tronic, T.; Clendenning, S.; Fischer, P.; Putna, E. S.; Radosavljevic, M.; et al. Process Integration and Future Outlook of 2D Transistors. *Nat. Commun.* **2023**, *14*, 6400.

(3) Das, S.; Sebastian, A.; Pop, E.; McClellan, C. J.; Franklin, A. D.; Grasser, T.; Knobloch, T.; Illarionov, Y.; Penumatcha, A. V.; Appenzeller, J.; Chen, Z.; Zhu, W.; Asselberghs, I.; Li, L.-J.; Avci, U. E.; Bhat, N.; Anthopoulos, T. D.; Singh, R. Transistors Based on Two-Dimensional Materials for Future Integrated Circuits. *Nat. Electron.* **2021**, *4*, 786−799.

(4) English, C. D.; Smithe, K. K. H.; Xu, R. L.; Pop, E. Approaching Ballistic Transport in Monolayer MoS_2 Transistors with Self-Aligned 10 Top Gates. *2016 IEEE International Electron Devices Meeting (IEDM)*; IEEE, 2016; pp 5.6.1−5.6.4.

(5) Xia, Y.; Chen, X.; Wei, J.; Wang, S.; Chen, S.; Wu, S.; Ji, M.; Sun, Z.; Xu, Z.; Bao, W.; Zhou, P. 12-Inch Growth of Uniform MoS_2 Monolayer for Integrated Circuit Manufacture. *Nat. Mater.* **2023**, *22*, 1324−1331.

(6) Wan, Y.; Li, E.; Yu, Z.; Huang, J.-K.; Li, M.-Y.; Chou, A.-S.; Lee, Y.-T.; Lee, C.-J.; Hsu, H.-C.; Zhan, Q.; Aljarb, A.; Fu, J.-H.; Chiu, S.-P.; Wang, X.; Lin, J.-J.; Chiu, Y.-P.; Chang, W.-H.; Wang, H.; Shi, Y.; Lin, N.; et al. Low-Defect-Density WS_2 by Hydroxide Vapor Phase Deposition. *Nat. Commun.* **2022**, *13*, 4149.

(7) Wang, J.; Xu, X.; Cheng, T.; Gu, L.; Qiao, R.; Liang, Z.; Ding, D.; Hong, H.; Zheng, P.; Zhang, Z.; Zhang, Z.; Zhang, S.; Cui, G.; Chang, C.; Huang, C.; Qi, J.; Liang, J.; Liu, C.; Zuo, Y.; Xue, G.; et al. Dual-Coupling-Guided Epitaxial Growth of Wafer-Scale Single-Crystal WS_2 Monolayer on Vicinal a-Plane Sapphire. *Nat. Nanotechnol.* **2022**, *17*, 33−38.

(8) Qin, Z.; Loh, L.; Wang, J.; Xu, X.; Zhang, Q.; Haas, B.; Alvarez, C.; Okuno, H.; Yong, J. Z.; Schultz, T.; Koch, N.; Dan, J.; Pennycook, S. J.; Zeng, D.; Bosman, M.; Eda, G. Growth of Nb-Doped Monolayer WS_2 by Liquid-Phase Precursor Mixing. *ACS Nano* **2019**, *13*, 10768−10775.

(9) Zhang, F.; Zheng, B.; Sebastian, A.; Olson, D. H.; Liu, M.; Fujisawa, K.; Pham, Y. T. H.; Jimenez, V. O.; Kalappattil, V.; Miao, L.; Zhang, T.; Pendurthi, R.; Lei, Y.; Elías, A. L.; Wang, Y.; Alem, N.; Hopkins, P. E.; Das, S.; Crespi, V. H.; Phan, M.-H.; et al. Monolayer Vanadium-Doped Tungsten Disulfide: A Room-Temperature Dilute Magnetic Semiconductor. *Adv. Sci.* **2020**, *7*, 2001174.

(10) Yun, S. J.; Duong, D. L.; Ha, D. M.; Singh, K.; Phan, T. L.; Choi, W.; Kim, Y.-M.; Lee, Y. H. Ferromagnetic Order at Room Temperature in Monolayer WSe_2 Semiconductor *via* Vanadium Dopant. *Adv. Sci.* **2020**, *7*, 1903076.

(11) Li, S.; Hong, J.; Gao, B.; Lin, Y.-C.; Lim, H. E.; Lu, X.; Wu, J.; Liu, S.; Tateyama, Y.; Sakuma, Y.; Tsukagoshi, K.; Suenaga, K.; Taniguchi, T. Tunable Doping of Rhenium and Vanadium into Transition Metal Dichalcogenides for Two-Dimensional Electronics. *Adv. Sci.* **2021**, *8*, No. e2004438.

(12) Loh, L.; Chen, Y.; Wang, J.; Yin, X.; Tang, C. S.; Zhang, Q.; Watanabe, K.; Taniguchi, T.; Wee, A. T.; Bosman, M.; Quek, S. Y.; Eda, G. Impurity-Induced Emission in Re-Doped WS_2 Monolayers. *Nano Lett.* **2021**, *21*, 5293−5300.

(13) Li, T.; Guo, W.; Ma, L.; Li, W.; Yu, Z.; Han, Z.; Gao, S.; Liu, L.; Fan, D.; Wang, Z.; Yang, Y.; Lin, W.; Luo, Z.; Chen, X.; Dai, N.; Tu, X.; Pan, D.; Yao, Y.; Wang, P.; Nie, Y.; et al. Epitaxial Growth of Wafer-Scale Molybdenum Disulfide Semiconductor Single Crystals on Sapphire. *Nat. Nanotechnol.* **2021**, *16*, 1201−1207.

(14) Smithe, K. K. H.; Suryavanshi, S. V.; Muñoz Rojo, M.; Tedjarati, A. D.; Pop, E. Low Variability in Synthetic Monolayer MoS_2 Devices. *ACS Nano* **2017**, *11*, 8456−8463.

(15) Fu, S.; Kang, K.; Shayan, K.; Yoshimura, A.; Dadras, S.; Wang, X.; Zhang, L.; Chen, S.; Liu, N.; Jindal, A.; Li, X.; Pasupathy, A. N.; Vamivakas, A. N.; Meunier, V.; Strauf, S.; Yang, E. H. Enabling Room Temperature Ferromagnetism in Monolayer MoS2 via in Situ Iron-Doping. *Nat. Commun.* **2020**, *11*, 2034.

(16) Azizi, A.; Wang, Y.; Lin, Z.; Wang, K.; Elias, A. L.; Terrones, M.; Crespi, V. H.; Alem, N. Spontaneous Formation of Atomically Thin Stripes in Transition Metal Dichalcogenide Monolayers. *Nano Lett.* **2016**, *16*, 6982−6987.

(17) Xue, G.; Sui, X.; Yin, P.; Zhou, Z.; Li, X.; Cheng, Y.; Guo, Q.; Zhang, S.; Wen, Y.; Zuo, Y.; Zhao, C.; Wu, M.; Gao, P.; Li, Q.; He, J.; Wang, E.; Zhang, G.; Liu, C.; Liu, K. Modularized Batch Production of 12-Inch Transition Metal Dichalcogenides by Local Element Supply. *Sci. Bull.* **2023**, *68*, 1514−1521.

(18) Suenaga, K.; Ji, H. G.; Lin, Y.-C.; Vincent, T.; Maruyama, M.; Aji, A. S.; Shiratsuchi, Y.; Ding, D.; Kawahara, K.; Okada, S.; Panchal, V.; Kazakova, O.; Hibino, H.; Suenaga, K.; Ago, H. Surface-Mediated Aligned Growth of Monolayer MoS_2 and In-Plane Heterostructures with Graphene on Sapphire. *ACS Nano* **2018**, *12*, 10032−10044.

(19) Wang, S.; Rong, Y.; Fan, Y.; Pacios, M.; Bhaskaran, H.; He, K.; Warner, J. H. Shape Evolution of Monolayer MoS_2 Crystals Grown by Chemical Vapor Deposition. *Chem. Mater.* **2014**, *26*, 6371−6379.

(20) Yu, H.; Liao, M.; Zhao, W.; Liu, G.; Zhou, X. J.; Wei, Z.; Xu, X.; Liu, K.; Hu, Z.; Deng, K.; Zhou, S.; Shi, J.-A.; Gu, L.; Shen, C.; Zhang, T.; Du, L.; Xie, L.; Zhu, J.; Chen, W.; Yang, R.; et al. Wafer-Scale Growth and Transfer of Highly-Oriented Monolayer MoS_2 Continuous Films. *ACS Nano* **2017**, *11*, 12001−12007.

(21) Wang, Q.; Li, N.; Tang, J.; Zhu, J.; Zhang, Q.; Jia, Q.; Lu, Y.; Wei, Z.; Yu, H.; Zhao, Y.; Guo, Y.; Gu, L.; Sun, G.; Yang, W.; Yang,

https://doi.org/10.1021/acsnano.4c02164
ACS Nano 2024, 18, 25414−25424

R.; Shi, D.; Zhang, G. Wafer-Scale Highly Oriented Monolayer MoS_2 with Large Domain Sizes. *Nano Lett.* **2020**, *20*, 7193−7199.
(22) Ling, X.; Lee, Y.-H.; Lin, Y.; Fang, W.; Yu, L.; Dresselhaus, M. S.; Kong, J. Role of the Seeding Promoter in MoS_2 Growth by Chemical Vapor Deposition. *Nano Lett.* **2014**, *14*, 464−472.
(23) Zhou, J.; Lin, J.; Huang, X.; Zhou, Y.; Chen, Y.; Xia, J.; Wang, H.; Xie, Y.; Yu, H.; Lei, J.; Wu, D.; Liu, F.; Fu, Q.; Zeng, Q.; Hsu, C.-H.; Yang, C.; Lu, L.; Yu, T.; Shen, Z.; Lin, H.; et al. A Library of Atomically Thin Metal Chalcogenides. *Nature* **2018**, *556*, 355−359.
(24) Zhang, P.; Wang, X.; Jiang, H.; Zhang, Y.; He, Q.; Si, K.; Li, B.; Zhao, F.; Cui, A.; Wei, Y.; Liu, L.; Que, H.; Tang, P.; Hu, Z.; Zhou, W.; Wu, K.; Gong, Y. Flux-Assisted Growth of Atomically Thin Materials. *Nat. Synth.* **2022**, *1*, 864−872.
(25) Kang, K.; Xie, S.; Huang, L.; Han, Y.; Huang, P. Y.; Mak, K. F.; Kim, C.-J.; Muller, D.; Park, J. High-Mobility Three-Atom-Thick Semiconducting Films with Wafer-Scale Homogeneity. *Nature* **2015**, *520*, 656−660.
(26) Park, J.-H.; Lu, A.-Y.; Shen, P.-C.; Shin, B. G.; Wang, H.; Mao, N.; Xu, R.; Jung, S. J.; Ham, D.; Kern, K.; Han, Y.; Kong, J. Synthesis of High-Performance Monolayer Molybdenum Disulfide at Low Temperature. *Small Methods* **2021**, *5*, No. e2000720.
(27) Hoang, A. T.; Hu, L.; Kim, B. J.; Van, T. T. N.; Park, K. D.; Jeong, Y.; Lee, K.; Ji, S.; Hong, J.; Katiyar, A. K.; Shong, B.; Kim, K.; Im, S.; Chung, W. J.; Ahn, J.-H. Low-Temperature Growth of MoS_2 on Polymer and Thin Glass Substrates for Flexible Electronics. *Nat. Nanotechnol.* **2023**, *18*, 1439−1447.
(28) Zhu, J.; Park, J.-H.; Vitale, S. A.; Ge, W.; Jung, G. S.; Wang, J.; Mohamed, M.; Zhang, T.; Ashok, M.; Xue, M.; Zheng, X.; Wang, Z.; Hansryd, J.; Chandrakasan, A. P.; Kong, J.; Palacios, T. Low-Thermal-Budget Synthesis of Monolayer Molybdenum Disulfide for Silicon Back-End-of-Line Integration on a 200 mm Platform. *Nat. Nanotechnol.* **2023**, *18*, 456−463.
(29) Kim, H.; Ovchinnikov, D.; Deiana, D.; Unuchek, D.; Kis, A. Suppressing Nucleation in Metal-Organic Chemical Vapor Deposition of MoS_2 Monolayers by Alkali Metal Halides. *Nano Lett.* **2017**, *17*, 5056−5063.
(30) Kim, T. S.; Dhakal, K. P.; Park, E.; Noh, G.; Chai, H.-J.; Kim, Y.; Oh, S.; Kang, M.; Park, J.; Kim, J.; Kim, S.; Jeong, H. Y.; Bang, S.; Kwak, J. Y.; Kim, J.; Kang, K. Gas-Phase Alkali Metal-Assisted MOCVD Growth of 2D Transition Metal Dichalcogenides for Large-Scale Precise Nucleation Control. *Small* **2022**, *18*, No. e2106368.
(31) Mun, J.; Park, H.; Park, J.; Joung, D.; Lee, S.-K.; Leem, J.; Myoung, J.-M.; Park, J.; Jeong, S.-H.; Chegal, W.; Nam, S.; Kang, S.-W. High-Mobility MoS2 Directly Grown on Polymer Substrate with Kinetics-Controlled Metal−Organic Chemical Vapor Deposition. *ACS Appl. Electron. Mater.* **2019**, *1*, 608−616.
(32) Zhang, K.; Bersch, B. M.; Zhang, F.; Briggs, N. C.; Subramanian, S.; Xu, K.; Chubarov, M.; Wang, K.; Lerach, J. O.; Redwing, J. M.; Fullerton-Shirey, S. K.; Terrones, M.; Robinson, J. A. Considerations for Utilizing Sodium Chloride in Epitaxial Molybdenum Disulfide. *ACS Appl. Mater. Interfaces* **2018**, *10*, 40831−40837.
(33) Cohen, A.; Patsha, A.; Mohapatra, P. K.; Kazes, M.; Ranganathan, K.; Houben, L.; Oron, D.; Ismach, A. Growth-Etch Metal-Organic Chemical Vapor Deposition Approach of WS_2 Atomic Layers. *ACS Nano* **2021**, *15*, 526−538.
(34) Chubarov, M.; Choudhury, T. H.; Hickey, D. R.; Bachu, S.; Zhang, T.; Sebastian, A.; Bansal, A.; Zhu, H.; Trainor, N.; Das, S.; Terrones, M.; Alem, N.; Redwing, J. M. Wafer-Scale Epitaxial Growth of Unidirectional WS_2 Monolayers on Sapphire. *ACS Nano* **2021**, *15*, 2532−2541.
(35) Zhang, T.; Fujisawa, K.; Zhang, F.; Liu, M.; Lucking, M. C.; Gontijo, R. N.; Lei, Y.; Liu, H.; Crust, K.; Granzier-Nakajima, T.; Terrones, H.; Elías, A. L.; Terrones, M. Universal In Situ Substitutional Doping of Transition Metal Dichalcogenides by Liquid-Phase Precursor-Assisted Synthesis. *ACS Nano* **2020**, *14*, 4326−4335.
(36) Loh, L.; Zhang, Z.; Bosman, M.; Eda, G. Substitutional Doping in 2D Transition Metal Dichalcogenides. *Nano Res.* **2021**, *14*, 1668−1681.
(37) Zhao, W.; Ghorannevis, Z.; Chu, L.; Toh, M.; Kloc, C.; Tan, P.-H.; Eda, G. Evolution of Electronic Structure in Atomically Thin Sheets of WS_2 and WSe_2. *ACS Nano* **2013**, *7*, 791−797.
(38) Cadiz, F.; Courtade, E.; Robert, C.; Wang, G.; Shen, Y.; Cai, H.; Taniguchi, T.; Watanabe, K.; Carrere, H.; Lagarde, D.; Manca, M.; Amand, T.; Renucci, P.; Tongay, S.; Marie, X.; Urbaszek, B. Excitonic Linewidth Approaching the Homogeneous Limit in MoS_2-Based van Der Waals Heterostructures. *Phys. Rev. X* **2017**, *7*, 021026.
(39) Ly, T. H.; Chiu, M.-H.; Li, M.-Y.; Zhao, J.; Perello, D. J.; Cichocka, M. O.; Oh, H. M.; Chae, S. H.; Jeong, H. Y.; Yao, F.; Li, L.-J.; Lee, Y. H. Observing Grain Boundaries in CVD-Grown Monolayer Transition Metal Dichalcogenides. *ACS Nano* **2014**, *8*, 11401−11408.
(40) Zeng, H.; Liu, G.-B.; Dai, J.; Yan, Y.; Zhu, B.; He, R.; Xie, L.; Xu, S.; Chen, X.; Yao, W.; Cui, X. Optical Signature of Symmetry Variations and Spin-Valley Coupling in Atomically Thin Tungsten Dichalcogenides. *Sci. Rep.* **2013**, *3*, 1608.
(41) Ma, Z.; Wang, S.; Deng, Q.; Hou, Z.; Zhou, X.; Li, X.; Cui, F.; Si, H.; Zhai, T.; Xu, H. Epitaxial Growth of Rectangle Shape MoS_2 with Highly Aligned Orientation on Twofold Symmetry a-Plane Sapphire. *Small* **2020**, *16*, 2000596.
(42) Rodriguez, A.; Velický, M.; Ř́ahová, J.; Zólyomi, V.; Koltai, J.; Kalbáč, M.; Frank, O. Activation of Raman Modes in Monolayer Transition Metal Dichalcogenides through Strong Interaction with Gold. *Phys. Rev. B* **2022**, *105*, 195413.
(43) Cheng, Z.; Pang, C.-S.; Wang, P.; Le, S. T.; Wu, Y.; Shahrjerdi, D.; Radu, I.; Lemme, M. C.; Peng, L.-M.; Duan, X.; Chen, Z.; Appenzeller, J.; Koester, S. J.; Pop, E.; Franklin, A. D.; Richter, C. A. How to Report and Benchmark Emerging Field-Effect Transistors. *Nat. Electron.* **2022**, *5*, 416−423.
(44) Cui, Y.; Xin, R.; Yu, Z.; Pan, Y.; Ong, Z.-Y.; Wei, X.; Wang, J.; Nan, H.; Ni, Z.; Wu, Y.; Chen, T.; Shi, Y.; Wang, B.; Zhang, G.; Zhang, Y.-W.; Wang, X. High-Performance Monolayer WS_2 Field-Effect Transistors on High-κ Dielectrics. *Adv. Mater.* **2015**, *27*, 5230−5234.
(45) Wang, Y.; Kim, J. C.; Wu, R. J.; Martinez, J.; Song, X.; Yang, J.; Zhao, F.; Mkhoyan, A.; Jeong, H. Y.; Chhowalla, M. Van Der Waals Contacts between Three-Dimensional Metals and Two-Dimensional Semiconductors. *Nature* **2019**, *568*, 70−74.
(46) Shen, P.-C.; Su, C.; Lin, Y.; Chou, A.-S.; Cheng, C.-C.; Park, J.-H.; Chiu, M.-H.; Lu, A.-Y.; Tang, H.-L.; Tavakoli, M. M.; Pitner, G.; Ji, X.; Cai, Z.; Mao, N.; Wang, J.; Tung, V.; Li, J.; Bokor, J.; Zettl, A.; Wu, C.-I.; et al. Ultralow Contact Resistance between Semimetal and Monolayer Semiconductors. *Nature* **2021**, *593*, 211−217.
(47) Liu, Y.; Guo, J.; Zhu, E.; Liao, L.; Lee, S.-J.; Ding, M.; Shakir, I.; Gambin, V.; Huang, Y.; Duan, X. Approaching the Schottky-Mott Limit in van Der Waals Metal-Semiconductor Junctions. *Nature* **2018**, *557*, 696−700.
(48) Zou, J.; Xu, Y.; Miao, X.; Chen, H.; Zhang, R.; Tan, J.; Tang, L.; Cai, Z.; Zhang, C.; Kang, L.; Zhang, X.; Ma, C.; Cheng, H.-M.; Liu, B. Raman Spectroscopy and Carrier Scattering in 2D Tungsten Disulfides with Vanadium Doping. *Mater. Chem. Front.* **2023**, *7*, 2059−2067.
(49) Kozhakhmetov, A.; Schuler, B.; Tan, A. M. Z.; Cochrane, K. A.; Nasr, J. R.; El-Sherif, H.; Bansal, A.; Vera, A.; Bojan, V.; Redwing, J. M.; Bassim, N.; Das, S.; Hennig, R. G.; Weber-Bargioni, A.; Robinson, J. A. Scalable Substitutional Re-Doping and Its Impact on the Optical and Electronic Properties of Tungsten Diselenide. *Adv. Mater.* **2020**, *32*, No. e2005159.
(50) Gong, Y.; Lin, J.; Wang, X.; Shi, G.; Lei, S.; Lin, Z.; Zou, X.; Ye, G.; Vajtai, R.; Yakobson, B. I.; Terrones, H.; Terrones, M.; Tay, B. K.; Lou, J.; Pantelides, S. T.; Liu, Z.; Zhou, W.; Ajayan, P. M. Vertical and In-Plane Heterostructures from WS_2/MoS_2 Monolayers. *Nat. Mater.* **2014**, *13*, 1135−1142.
(51) Zheng, S.; Sun, L.; Yin, T.; Dubrovkin, A. M.; Liu, F.; Liu, Z.; Shen, Z. X.; Fan, H. J. Monolayers of $W_xMo_{1-x}S_2$ Alloy Heterostructure with in-Plane Composition Variations. *Appl. Phys. Lett.* **2015**, *106*, 063113.

https://doi.org/10.1021/acsnano.4c02164
ACS Nano 2024, 18, 25414−25424

(52) Ortiz-Conde, A.; García Sánchez, F. J.; Liou, J. J.; Cerdeira, A.; Estrada, M.; Yue, Y. A Review of Recent MOSFET Threshold Voltage Extraction Methods. *Microelectron. Reliab.* **2002**, *42*, 583−596.

https://doi.org/10.1021/acsnano.4c02164
ACS Nano 2024, 18, 25414−25424

Supporting Information for "Chemically Tailored Growth of 2D Semiconductors *via* Hybrid Metal-Organic Chemical Vapor Deposition"

Zhepeng Zhang[1,#], Lauren Hoang[2,#], Marisa Hocking[1], Zhenghan Peng[1], Jenny Hu[3], Gregory Zaborski Jr.[1], Pooja Reddy[1], Johnny Dollard[1], David Goldhaber-Gordon[4,5], Tony F. Heinz[3,5,6], Eric Pop[1,2,7], Andrew J. Mannix[1,5]*

[1]Department of Materials Science & Engineering, Stanford University, Stanford, CA 94305, USA
[2]Department of Electrical Engineering, Stanford University, Stanford, CA 94305, USA
[3]Department of Applied Physics, Stanford University, Stanford, CA 94305, USA
[4]Department of Physics, Stanford University, Stanford, CA 94305, USA
[5]Stanford Institute for Materials and Energy Sciences, SLAC National Accelerator Laboratory, Menlo Park, CA 94025, USA
[6]Department of Photon Sciences, Stanford University, Stanford, CA 94305, USA
[7]Precourt Institute for Energy, Stanford University, Stanford, CA 94305, USA

*Corresponding author: A.J.M., ajmannix@stanford.edu

#These authors contributed equally to this work (Z.Z., L.H.).

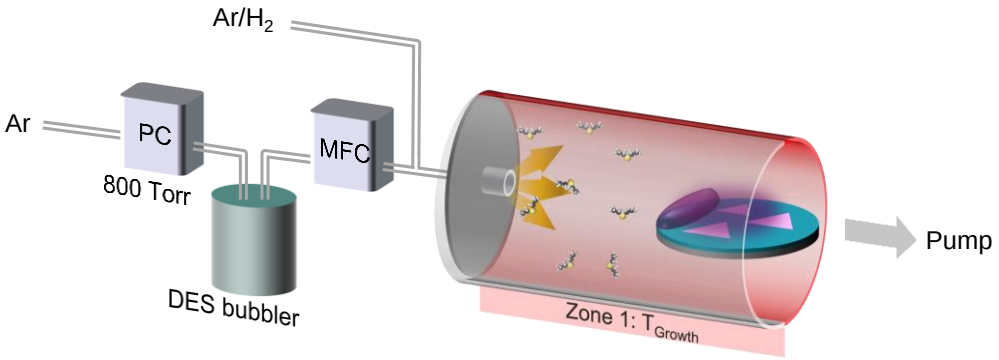

Figure S1. Schematic of Hy-MOCVD setup. PC and MFC denote pressure controller and mass flow controller, respectively.

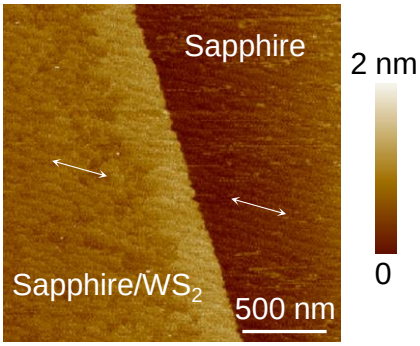

Figure S2. High magnification AFM image of spin-coating Hy-MOCVD WS_2 on *c*-plane sapphire substrate. Arrows highlight the directions of steps visible in sapphire/WS_2 and sapphire regions.

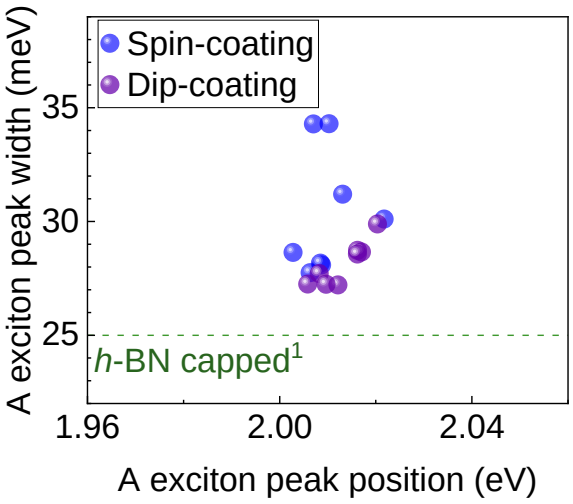

Figure S3. Fitted A exciton PL peak position versus peak width of as-grown spin-coating and dip-coating Hy-MOCVD WS_2. The Hy-MOCVD WS_2 monolayers present narrow A peak width distribution close to the *h*-BN capped WS_2.[1]

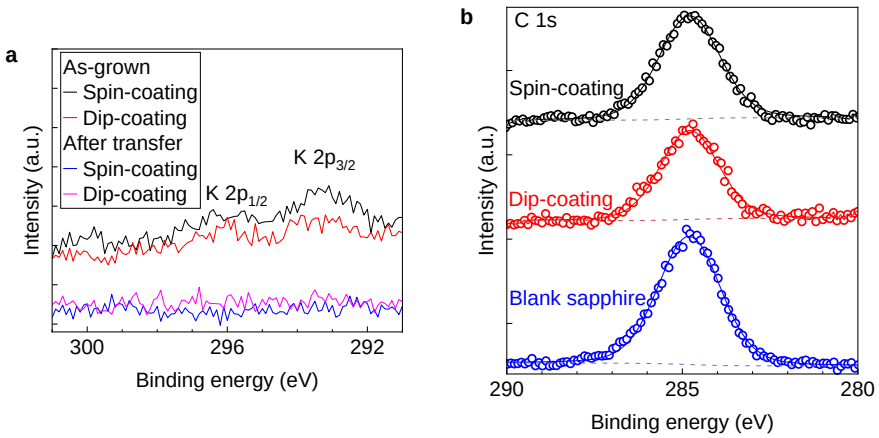

Figure S4. (a) High-resolution XPS spectra for the K 2p core level on Hy-MOCVD, before and after transfer, for both spin-coating and dip-coating precursor delivery. (b) C 1s core level spectra comparing a bare sapphire wafer with Hy-MOCVD films grown from dip-coating and spin-coating precursor delivery, indicating the absence of additional carbon contamination from the Hy-MOCVD process (data points shown with accompanying Voight profile curve fits).

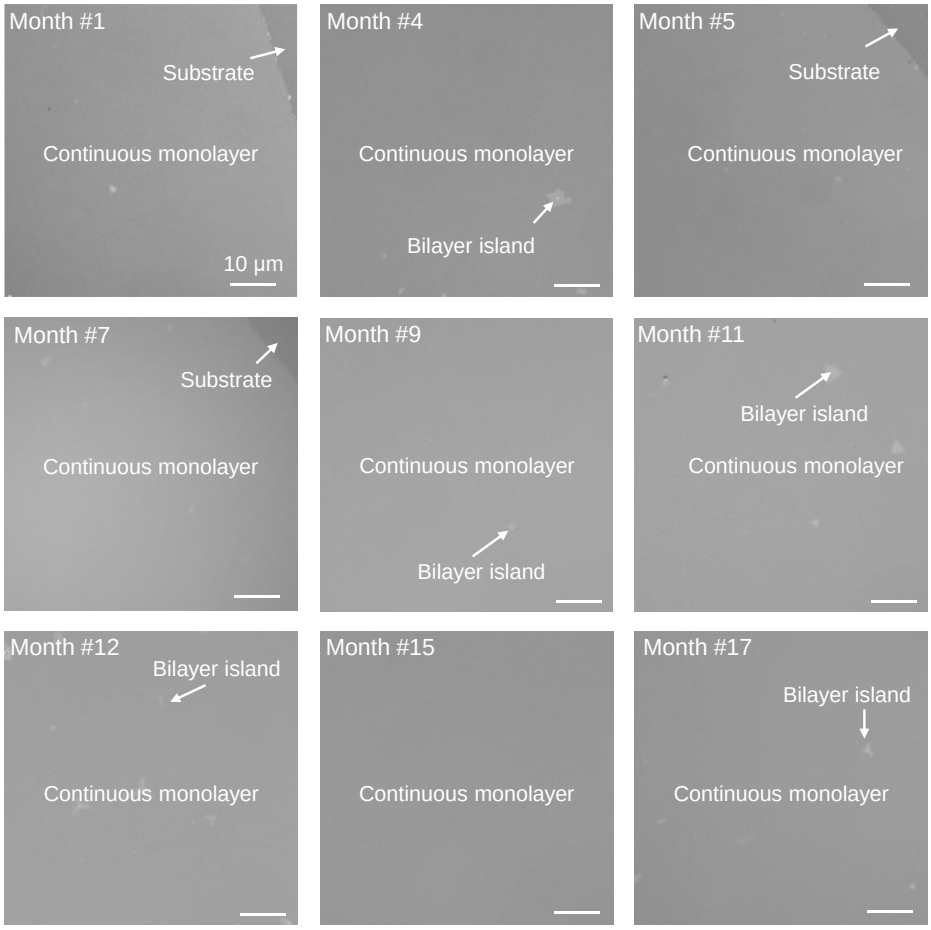

Figure S5. Optical images of dip-coating Hy-MOCVD grown monolayer WS_2 films on *c*-plane sapphire in 17 months. Scratch exposed substrate areas and bilayer islands on monolayer WS_2 are indicated. The parameters for these growths are identical. AMT + KOH (0.6 g + 0.05 g in 30 ml DI water) solution, 0.05 sccm DES, 1600 sccm Ar, 1 sccm H_2 and 775 °C growth temperature were used for the growth.

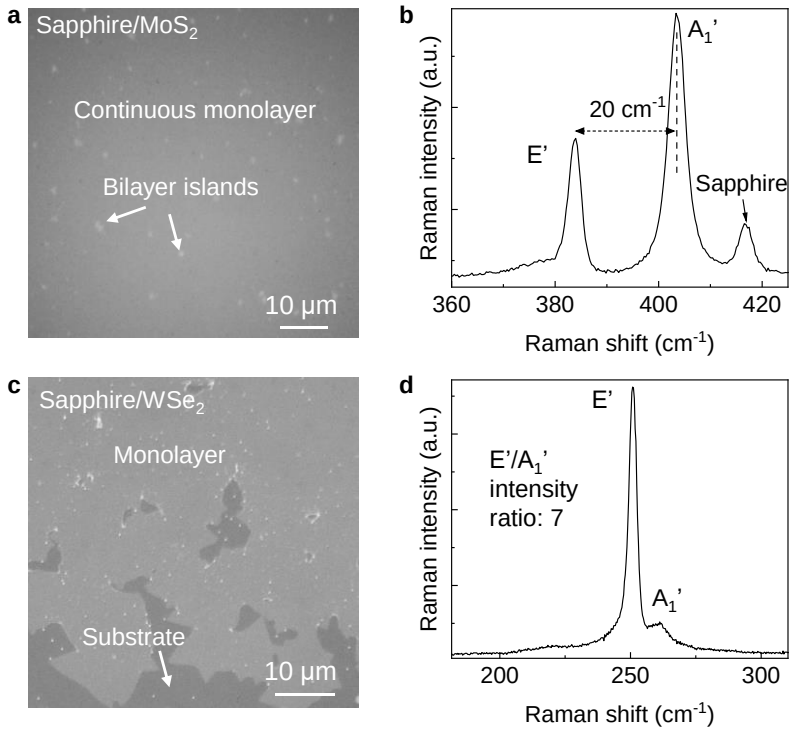

Figure S6. Optical images (a,c) and Raman spectra (b,d) of dip-coating Hy-MOCVD grown monolayer MoS_2 and WSe_2 films on *c*-plane sapphire substrates. The MoS_2 E' to A_1' peak distance of 20 cm^{-1} and the WSe_2 E'/A_1' peak intensity ratio of 7 indicate the predominantly monolayer character of Hy-MOCVD grown MoS_2 and WSe_2, respectively. Ammonium molybdate tetrahydrate and diisopropylselenium were used as Mo- and Se-sources for the Hy-MOCVD growth of MoS_2 and WSe_2, respectively.

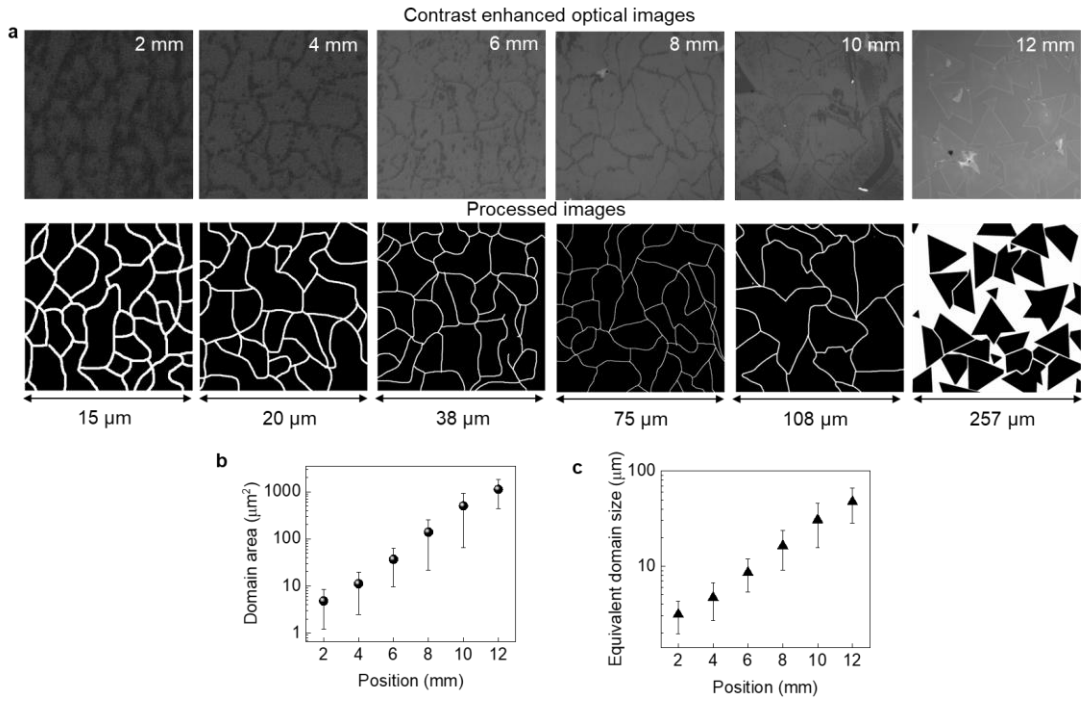

Figure S7. The domain size extraction of dip-coating Hy-MOCVD WS_2 continuous monolayer film on sapphire substrate. **(a)** Contrast enhanced optical images (top) and processed images of 7 min ozone etched WS_2 continuous monolayer films and domains on different positions 2-12 mm away from the dip-coating edge in dip-coating Hy-MOCVD. **(b)** Extracted domain areas versus position plot. **(c)** Equivalent domain size versus position plot. Particle analysis function in Image J was used to extract domain areas from processed images. The domain shape was assumed to be equilateral triangle for converting domain area to equivalent domain size (edge length of the equilateral triangle).

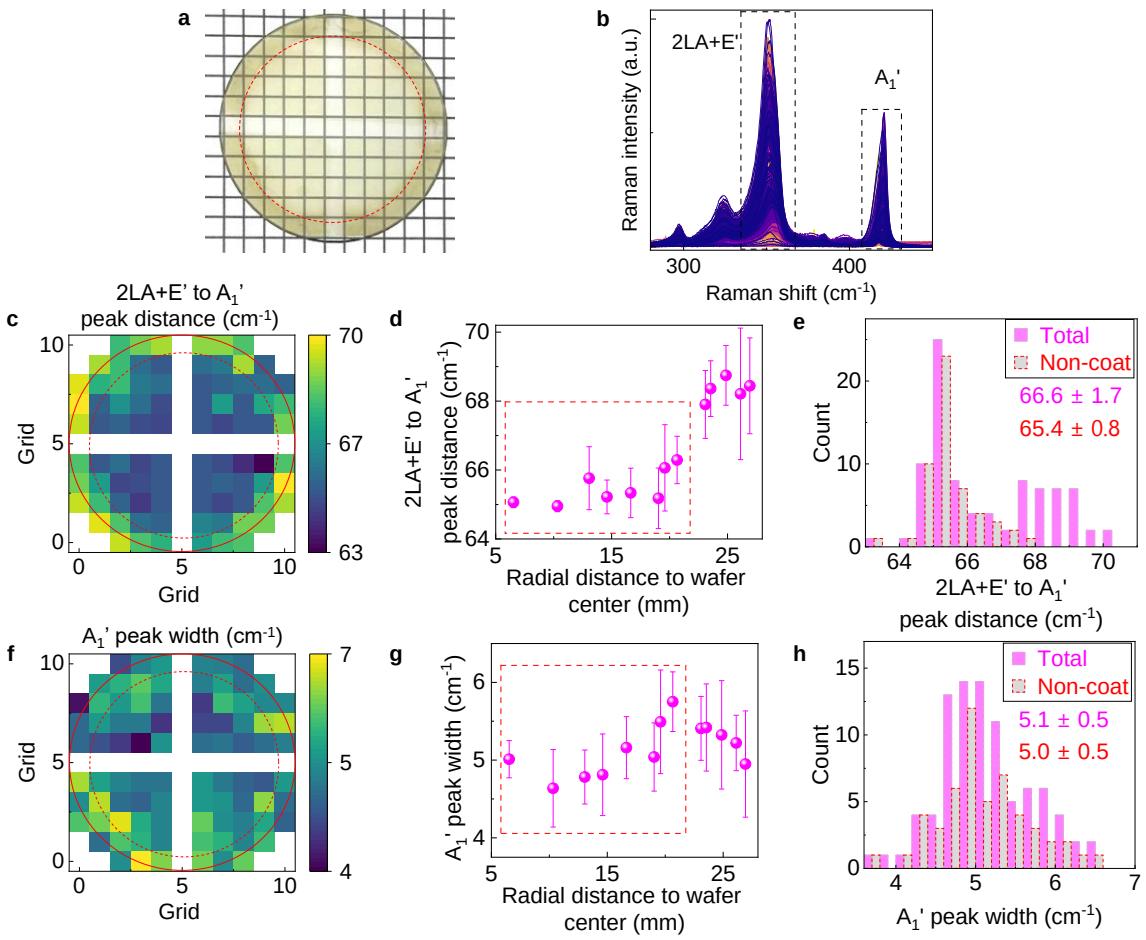

Figure S8. Raman map of Hy-MOCVD WS_2 on 2" sapphire wafer. (a) Photo of a 2" wafer on a grid paper. Red dashed circle highlights the WS_2 growth area during the Hy-MOCVD growth. (b) Raman spectra of 3×3 data points over 40×40 μm^2 area within each square of the total 88 squares on the wafer. The squares in the W trip covered area are excluded. The maps of 2LA+E' to A_1' peak distance (c) and A_1' peak width (f). The pixel intensities are the average values of the 9 spectra collected in each square. The red line and red dash line highlight the area of 2" wafer and non-dip-coated area. (d) and (g) show the average intensity and peak widths along the radius direction in (c) and (f), respectively. Note that the radial distance is calculated with respect to the grid coordinate, and therefore can exceed the 1" (25.4 mm) radius expected for a 2" (50.8 mm) diameter wafer. The error bars are standard deviations. (e) and (h) are histograms of the intensities in (c) and (f), respectively. Average values and standard deviations of all the pixels and the pixels in non-coated area are indicated. The peak positions and widths were extracted using Horiba LabSpec 6.

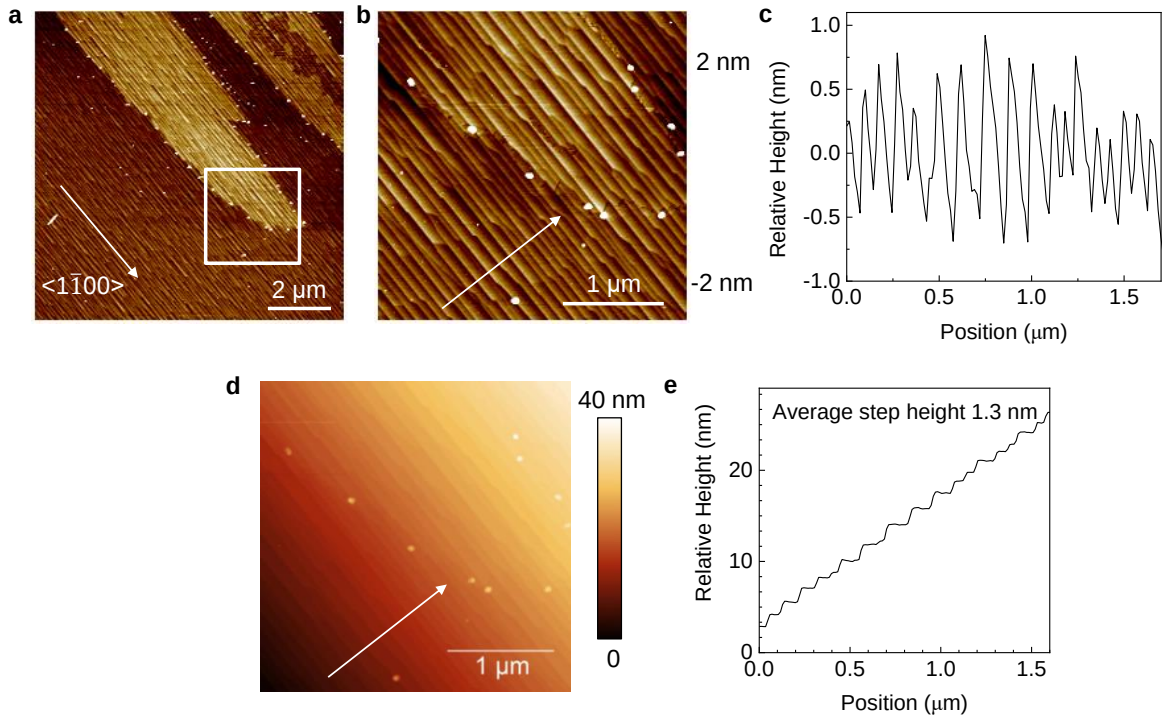

Figure S9. (a) AFM image of WS_2 ribbon grown on annealed *a*-plane sapphire wafer with terraces. **(b)** Zoomed in AFM image from the square in **(a)**. **(c)** Height line profile of sapphire wafer terraces along the white arrow in **(b)**. **(d)** Zoomed in AFM image from the square in **(a)**. **(e)** Height line profile of sapphire wafer terraces along the white arrow in **(d)**. **(a)** and **(b)** are flattened with NanoScope Analysis. **(d)** is flattened with Gwyddion.

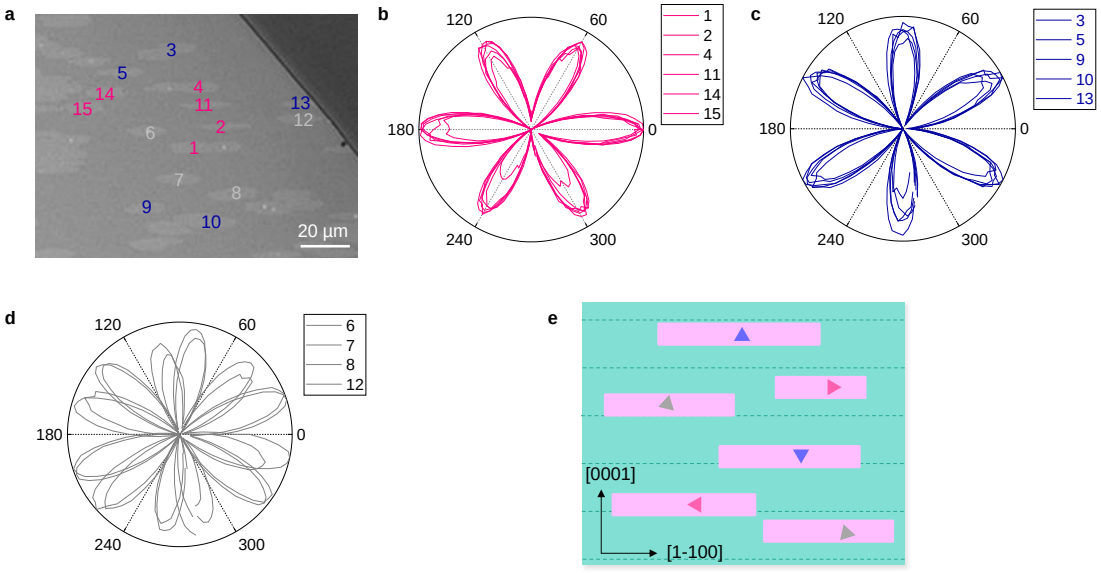

Figure S10. (a) Contrast-enhanced optical image of Hy-MOCVD grown WS_2 ribbons on annealed *a*-plane sapphire. **(b-d)** Polarization-resolved SHG of the ribbons highlighted in **(a)**. The SHG signals are normalized based on their maximum intensities. The armchair orientations of the WS_2 lattice within the ribbons are classified into three distinct groups: parallel (**b**), perpendicular (**c**), and randomly orientated (**d**) with respect to the long axis of the ribbon. **(e)** Schematic of WS_2 ribbons grown on an *a*-plane sapphire substrate featuring consistent ribbon orientation but varying lattice orientations. The corners of the triangles denote the armchair directions of the WS_2 lattice within the ribbon. Dashed lines indicate the terrace edge directions on the annealed *a*-plane sapphire.

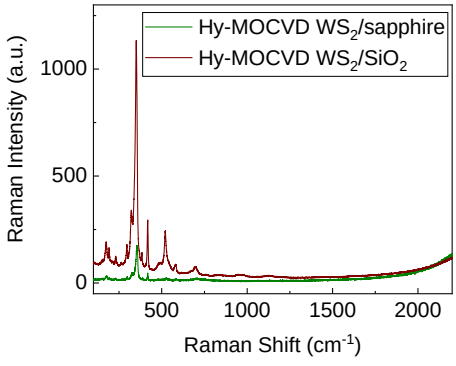

Figure S11. Raman spectra of as-grown Hy-MOCVD WS_2 on sapphire and SiO_2 showing no amorphous carbon signal.

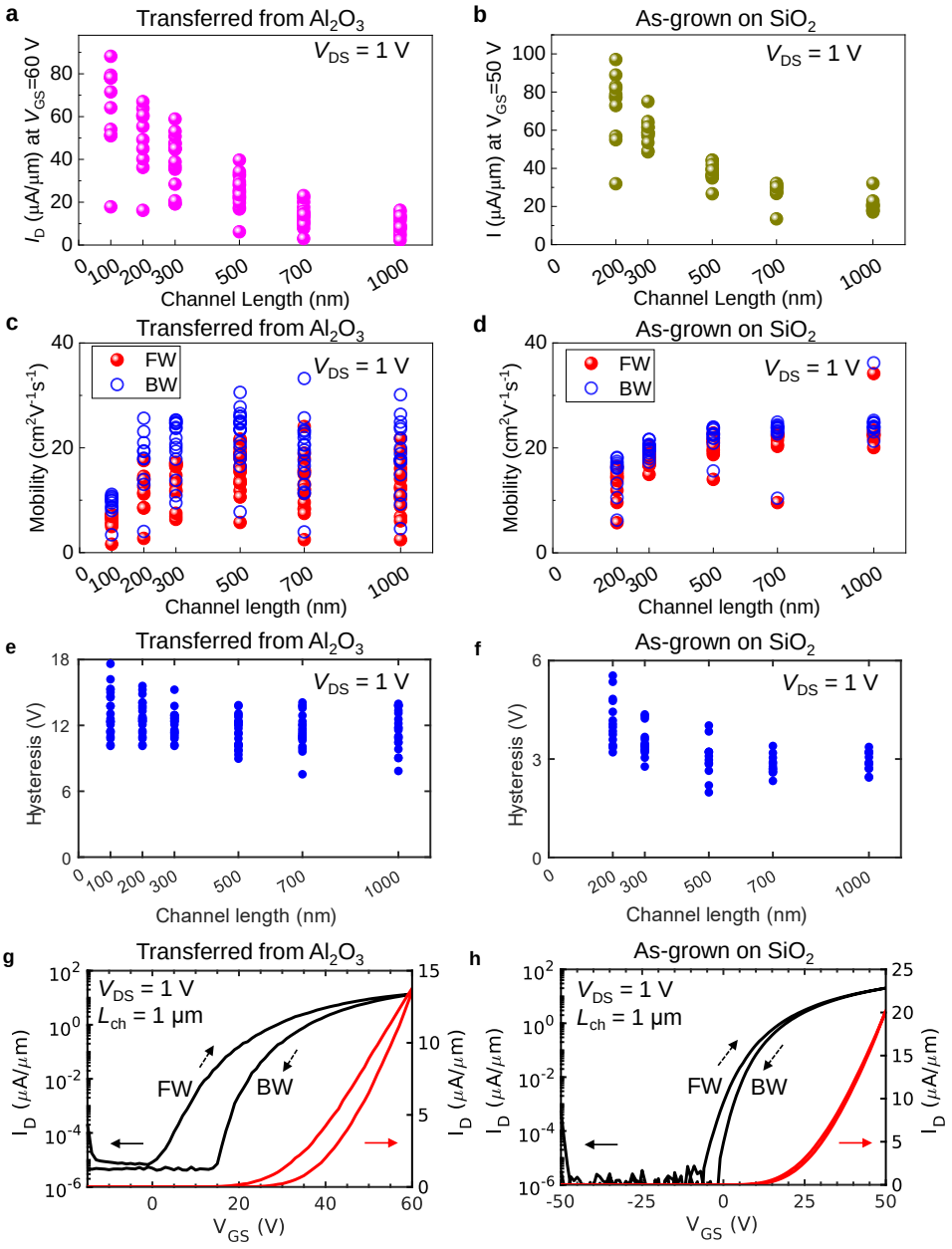

Figure S12. (a,b) On-state current (V_{DS} = 1 V) vs. channel length of FETs for transferred and as-grown Hy-MOCVD WS_2, respectively. **(c,d)** Estimated field-effect mobility vs. channel length of FETs for transferred and as-grown Hy-MOCVD WS_2, respectively. **(e,f)** Hysteresis vs. channel length of FETs for transferred and as-grown

Hy-MOCVD WS_2, respectively. **(g,h)** Repetitive I_D vs V_{GS} curves of FETs for transferred and as-grown Hy-MOCVD WS_2 showing typical clockwise hysteresis, respectively. FW and BW stand for forward and backward I_D vs V_{GS} curves, respectively.

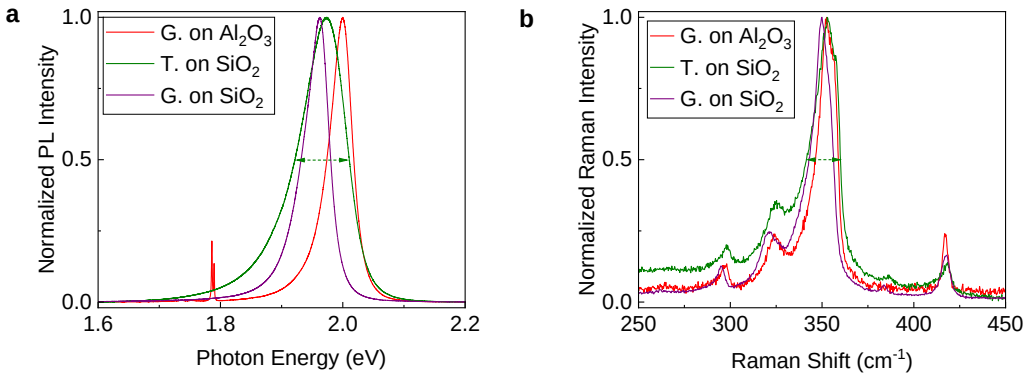

Figure S13. (a,b) PL and Raman spectrum comparison between as-grown Hy-MOCVD WS_2 on sapphire, transferred Hy-MOCVD WS_2 on from sapphire onto Si/SiO_2, and as-grown Hy-MOCVD WS_2 on Si/SiO_2. "G. on Al_2O_3" refers to "As-grown WS_2 on sapphire". "T. on SiO_2" is defined as "Transferred WS_2 from sapphire to SiO_2". "G. on SiO_2" is denoted as "As-grown WS_2 on SiO_2".

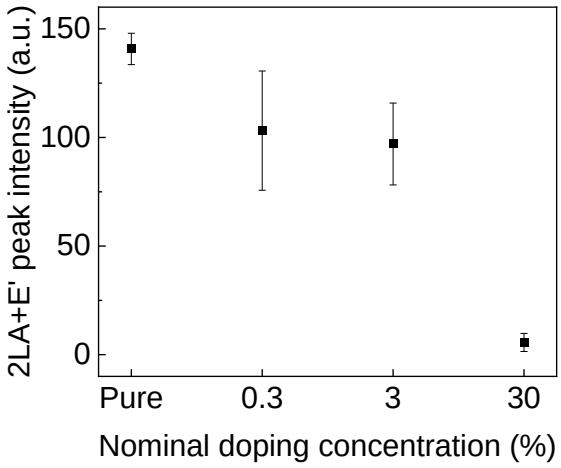

Figure S14. Raman 2LA+E' peak intensity versus nominal doping concentration plot of Hy-MOCVD grown V-doped WS_2.

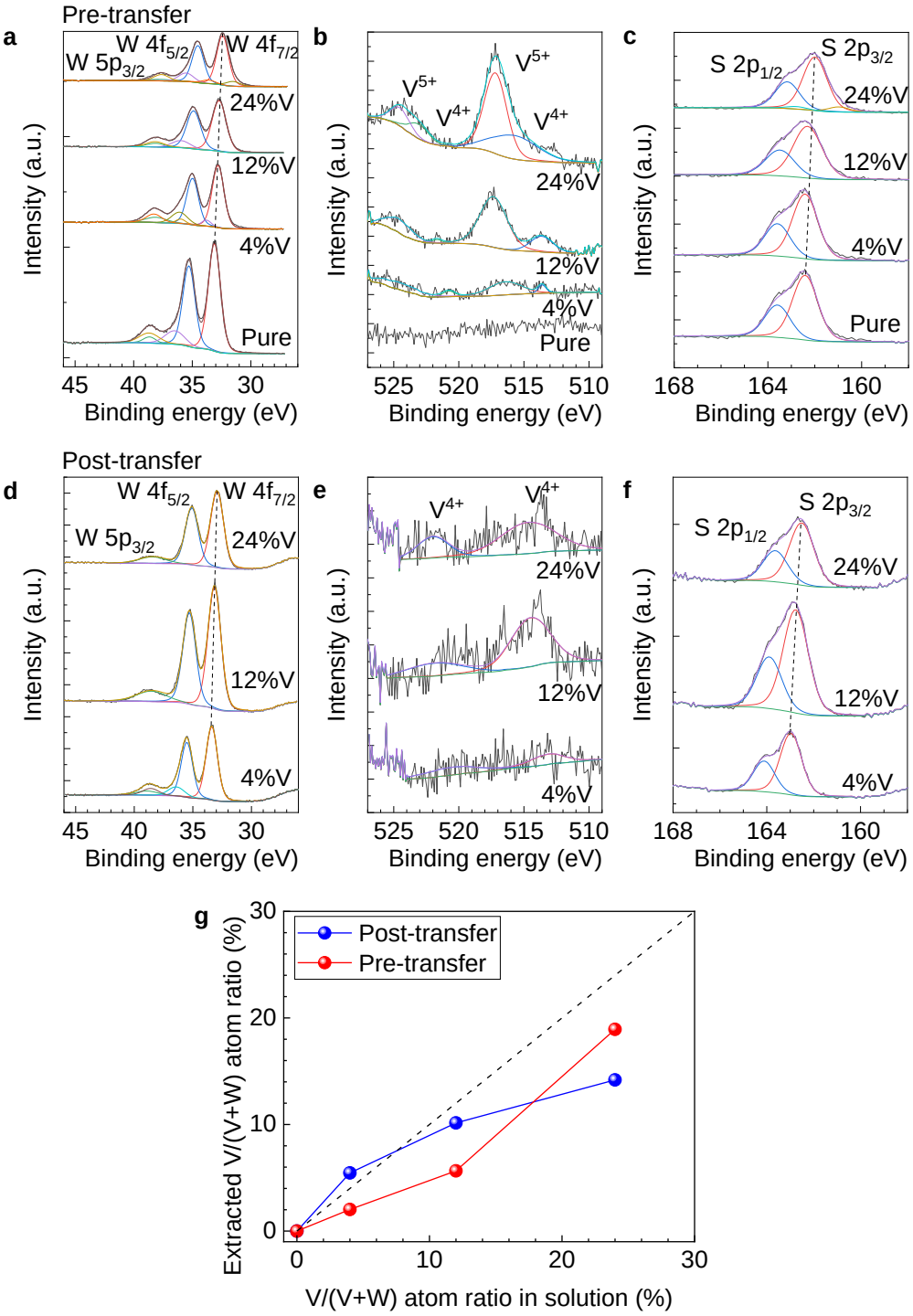

Figure S15. XPS characterization of Hy-MOCVD V-doped WS_2 before and after transfer. (a-c) High resolution XPS spectra of W 4f, V 2p and S 2p core levels for Hy-MOCVD V-doped WS_2 before transfer. (d-f) High resolution XPS spectra of W 4f, V 2p and S 2p core levels for Hy-MOCVD V-doped WS_2 after transfer. Black dashed lines in (a,c,d,f) connect the peak maxima for the undoped and 24%V samples to highlight the decreasing binding energy trend in W 4f and S 2p core levels. (g) Nominal V/(V+W) atom ratio in the precursor solution versus the ratio measured with XPS. The

measured XPS atomic ratio is calculated using the area of the V^{4+} component peak, because this is the expected chemical state for V substitution of W^{4+} in the WS_2 lattice. The samples were grown on *c*-plane sapphire for the pre-transfer measurements and transferred onto an Si/SiO_2 (100 nm) substrate for the post-transfer measurements. XPS peak fittings were completed on CasaXPS,[2] using the corrected relative sensitivity factors from the MultiPak XPS data processing software for the PHI VersaProbe 3 system. The residual standard deviations for V 2p fittings are in the range of 0.84~1.17. The W oxide states and V^{5+} states in pre-transfer samples can come from incomplete sulfurization of the W- and V- precursors. Their intensities are greatly reduced in the post-transfer samples, perhaps due to their water solubility or adhesion to the growth substrate.

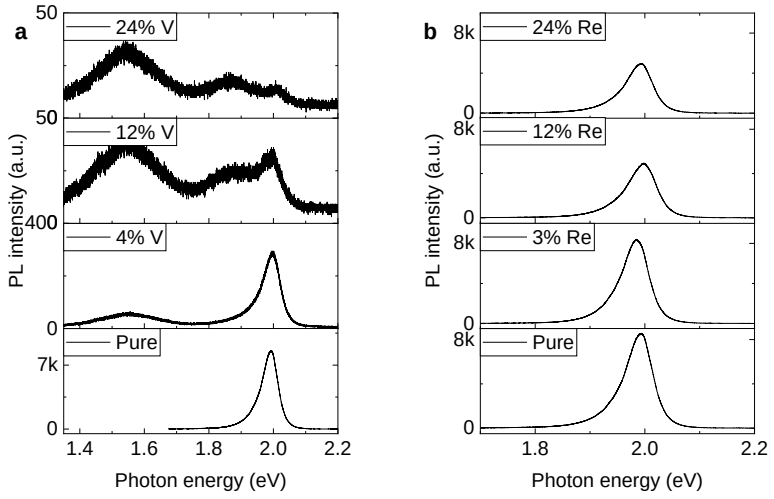

Figure S16. Series of photoluminescence spectra for Hy-MOCVD-grown V-doped (a) and Re-doped (b) WS_2 at room temperature. The samples were grown on sapphire and transferred to SiO_2 substrates. The dopant concentration values are given as the nominal dopant concentration in the solution and were deposited *via* spin coating.

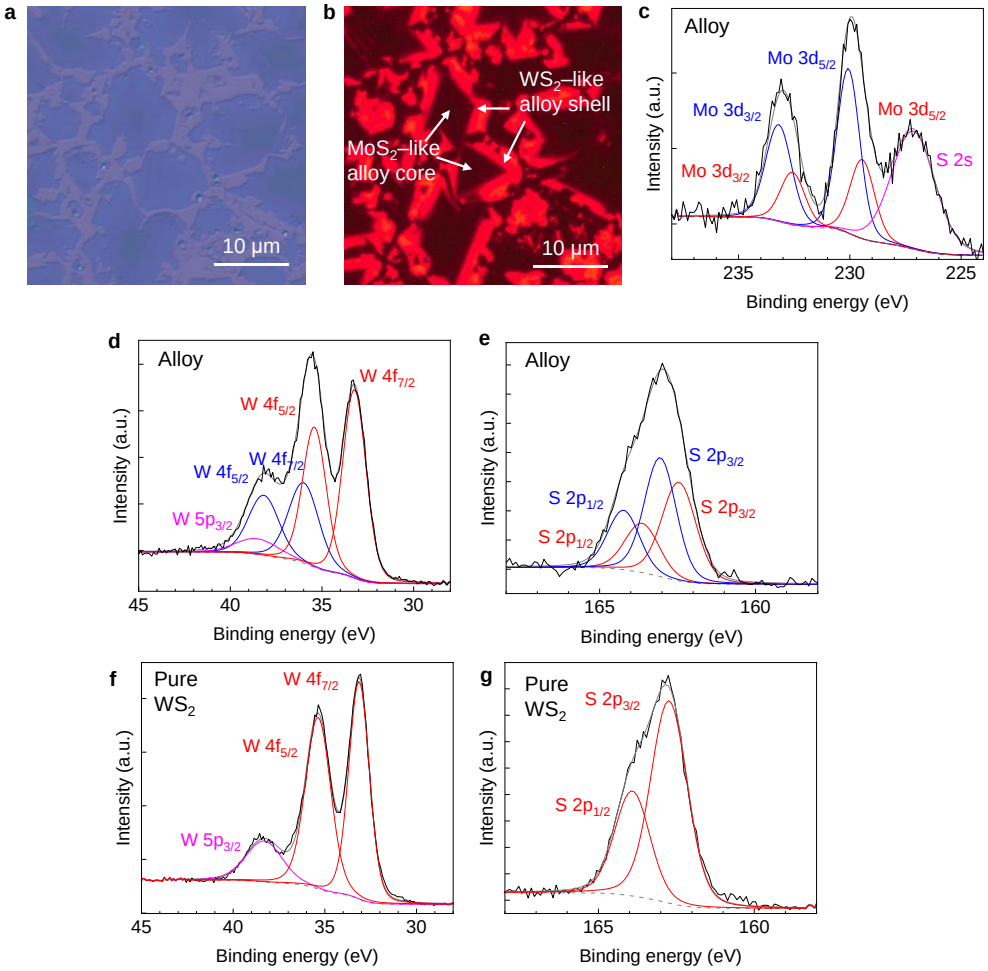

Figure S17. Characterization of $Mo_xW_{1-x}S_2$ alloy samples. (a) Optical microscope image (aperture stop applied) of transferred $Mo_xW_{1-x}S_2$ alloy grown with Mo/W mole ratio of ½ in the initial solution. (b) The fluorescence image of the transferred $Mo_xW_{1-x}S_2$ alloy in the same area of (a). (c-e) High-resolution XPS spectra of Mo 3d, W 4f and S 2p of as-grown $Mo_xW_{1-x}S_2$ alloy sample. (f-g) High-resolution XPS spectra of W 4f and S 2p of as-grown pure WS_2 sample. XPS peak fittings were completed on CasaXPS.[2]

Table S1. Summary of the metrics of SS-CVD, Hy-MOCVD and MOCVD.

Metrics	SS-CVD	Hy-MOCVD	MOCVD
Domain size	• *Non-epitaxial:* < 100 μm for isolated domains of MoS_2[3] and WS_2.[4] 2-5 μm for continuous film of MoS_2.[5,6] 100s μm for isolated domains of MoS_2[7] on sapphire (O_2 assisted) and WS_2 grown on Au foil[8] • *Unidirectional epitaxy:* 10-20 μm for isolated domains of MoS_2[9,10] and WS_2.[11] (closed epitaxial film)	3-30 μm for continuous film (**Figure S7**); ~60 μm for isolated domains (**Figure 3i**)	• *No growth promoter:* 100s nm for continuous film.[12,13] 20 μm for isolated domians.[14] • *Using growth promoter:* 100s nm for continuous film.[15–17] 1 μm ~ 30 μm for continuous film.[18,19] 60 μm for isolated domains.[20] • *Using water etchant:* 100s nm ~ 15 μm for isolated domains.[21] • *Using reverse flow:* 120 μm for isolated domains.[22] 100s nm for continuous film.[23]
Growth time	~0.5 hours	2-6 hours (**Figure 2** and **3**)	10 minutes - 30 hours (**Table S2**)
Repeatability	• *Conventional source delivery:* Small variations of source amount and position modify the growth result dramatically. • *Special oxide delivery:* Improved consistency in oxygen assisted MoS_2 growth.[6,24]	Consistency between the growth over 17 months (**Figure S5**)	Excellent repeatability (precisely controlled metal and chalcogen source deliveries).
Composition and doping control	Potential for large metal/chalcogen ratio variation for standard oxide delivery, MoS_2.[25]	Precisely controlled organochalcogen flow rate. Easy transition metal engineering for doping and alloying (**Figure 5**)	Each new precursor or dopant source requires either adding a new vapor-phase delivery line to the MOCVD system or swapping for an existing source, with potential for contamination and memory effects.

Uniformity	• *Conventional oxide delivery:* Shape and coverage vary in hundred micrometer length, MoS_2.[25] • *With special oxide delivery:* 2-4" wafer continuous film, MoS_2, oxygen assisted.[6,24] 12" wafer continuous film, MoS_2.[5] • *With salt promoter:* 2" wafer continuous film, WS_2.[11]	~80% of the growth area on 2" wafer is uniformly monolayer and usable for device fabrication (**Figure 3j** and **Figure S8**)	Excellent wafer scale uniformity[15,23,26]

Table S2. Comparison of MOCVD growth parameters in literature.

MX_2	**Heating (CW/HW)**	**T_{Gr} (°C)**	**t_{Gr}**	**Promoter**	**Precursors**	**Flow rate (sccm)**	**Special design**	**Ref.**
MoS_2, WS_2	CW	1000	10-18 min	-	$Mo(CO)_6$, $W(CO)_6$, H_2S	10^{-4}, 400	Nucleation + Ripening	26
WS_2	CW	1000	10-45 min	-	$W(CO)_6$, H_2S	10^{-4}, 400	Nucleation + Ripening	13
WS_2	HW	850	30-40 min	-	$W(CO)_6$, DTBS	10^{-7}, 10^{-4}	Water etching-growth	21
MoS_2	HW	320	2-14 h	-	$W(CO)_6$, $(C_2H_5)_2S$	0.1, 2	Backward flow	22
MoS_2	HW	300	<1 h	Spin NaCl	$Mo(CO)_6$, $(C_2H_5)_2S$	120, 80	Backward flow	23
MoS_2	HW	150	31 h	-	$Mo(CO)_6$+C_2H_6S	0.6	Mix Mo and S sources	12
MoS_2, WS_2	HW	550	26 h	NaCl powder	$Mo(CO)_6$, $W(CO)_6$, $(C_2H_5)_2S$	0.01, 0.01, 0.4	-	15
$MoSe_2$, WSe_2	CW	800	1.5 h	-	$Mo(CO)_6$, $W(CO)_6$, H_2Se	10^{-4}, 10^{-4}, 7	Nucleation + Ripening	14
MoS_2	CW	250	8 h	NaCl powder	$Mo(CO)_6$, H_2S	-	-	16

MoS_2	HW	700	1 h	-	$Mo(CO)_6$, $(C_2H_5)_2S$	0.02, 0.3-13.2	-	17
MoS_2	HW	800-1050	30 min	KI/NaCl powder	$Mo(CO)_6$, H_2S	10^{-4}, S-rich	-	20
MoS_2, WS_2, $MoSe_2$, WSe_2	HW	600	4 h	$C_3H_5NaO_2$	$Mo(CO)_6$, $W(CO)_6$, $(C_2H_5)_2S$, $(CH_3)_2Se$	1.2, 3.5, 0.4, 0.5	Gas phase Na-promoter	18
MoS_2	HW	900	1 h	NaCl powder	$Mo(CO)_6$, $(C_2H_5)_2S$	2, 4	-	19

Abbreviations: MX_2 stands for the TMDC composition of M as the transition metal (Mo, W), and X as the chalcogen (S, Se); CW and HW refer to cold wall and hot wall, respectively; T_{Gr} refers to growth temperature; t_{Gr} denotes growth time; Ref. stands for Reference.

Table S3. Performance comparison between Hy-MOCVD WS_2 FET devices and previous reports.

Ref.	**Method**	**Contacts**	**Gate Dielectric**	**Electron mobility μ_e ($cm^2V^{-1}s^{-1}$)**	**Max I_D (μA/μm) at V_{DS}= 1 V**	**L_{ch} (nm)**	**Current on/off ratio**
This work	Hy-MOCVD	Ni/Au	100 nm SiO_2	35 (max)	88 (max)	100-1000	10^8(max)
27	CVD	Au	100 nm SiO_2	-	10	600	10^7
28	CVD	Bi	100 nm SiN_x	18	300	100	-
29	CVD	Bi/Au	300 nm SiO_2	21	100	150	10^7
30	CVD	Bi/Au	100 nm SiNx	200	400	100	10^8
31	CVD	Bi/Ti/Au	16/30 nm SiO_2/Al_2O_3 + 31nm Al_2O_3 DG	15.5	46	320	10^{10}
32	CVD	Sb/Au or Bi/Au	100 nm SiN_x	30	243	135	10^8
33	CVD	Ni/Au	8 nm BeO	26	325	50	10^8

34	CVD	Ni	2.8 nm HfO_2 + 5.5 nm HfO_2 DG	-	225	140	-
35	CVD	Ni/Au	10 nm HfLaO	-	267	80	-
8	CVD	Ti/Au	290 nm SiO_2	2.00	3.3	3000	10^7
4	CVD		Ionic Liquid	0.46	5×10^{-3}	30000	10^2
11	CVD		-	1.60	-	-	-
36	CVD	Cr/Au	300 nm SiO_2	3.00	-	8000	10^8
37	CVD	Cr/Au	SiO_2	13.80	-	-	10^8
38	ALD	Ti/Au	20nm Al_2O_3	6.85	-	-	10^5
26	MOCVD	Ni/Au	50nm Al_2O_3	33	26	100	10^6
13	MOCVD	Ni/Au	50nm Al_2O_3	16	20	100	10^7

Abbreviations: Ref. stands for Reference; DG denotes Dual gate; - refers to no available data; μ_e stands for field-effect electron mobility reported in the reference; I_{on} denotes on-state current; L_{ch} refers to channel length.

REFERENCES

(1) Cadiz, F.; Courtade, E.; Robert, C.; Wang, G.; Shen, Y.; Cai, H.; Taniguchi, T.; Watanabe, K.; Carrere, H.; Lagarde, D.; Manca, M.; Amand, T.; Renucci, P.; Tongay, S.; Marie, X.; Urbaszek, B. Excitonic Linewidth Approaching the Homogeneous Limit in MoS_2-Based van Der Waals Heterostructures. *Phys. Rev. X* **2017**, *7*, 021026.

(2) Fairley, N.; Fernandez, V.; Richard-Plouet, M.; Guillot-Deudon, C.; Walton, J.; Smith, E.; Flahaut, D.; Greiner, M.; Biesinger, M.; Tougaard, S.; Morgan, D.; Baltrusaitis, J. Systematic and Collaborative Approach to Problem Solving Using X-Ray Photoelectron Spectroscopy. *Applied Surface Science Advances* **2021**, *5*, 100112.

(3) Ling, X.; Lee, Y.-H.; Lin, Y.; Fang, W.; Yu, L.; Dresselhaus, M. S.; Kong, J. Role of the Seeding Promoter in MoS_2 Growth by Chemical Vapor Deposition. *Nano Lett.* **2014**, *14*, 464–472.

(4) Zhang, Y.; Zhang, Y.; Ji, Q.; Ju, J.; Yuan, H.; Shi, J.; Gao, T.; Ma, D.; Liu, M.; Chen, Y.; Song, X.; Hwang, H. Y.; Cui, Y.; Liu, Z. Controlled Growth of High-Quality Monolayer WS_2 Layers on Sapphire and Imaging Its Grain Boundary. *ACS Nano* **2013**, *7*, 8963–8971.

(5) Xia, Y.; Chen, X.; Wei, J.; Wang, S.; Chen, S.; Wu, S.; Ji, M.; Sun, Z.; Xu, Z.; Bao, W.; Zhou, P. 12-Inch Growth of Uniform MoS_2 Monolayer for Integrated Circuit Manufacture. *Nat. Mater.* **2023**, *22*, 1324–1331.

(6) Yu, H.; Liao, M.; Zhao, W.; Liu, G.; Zhou, X. J.; Wei, Z.; Xu, X.; Liu, K.; Hu, Z.; Deng, K.; Zhou, S.; Shi, J.-A.; Gu, L.; Shen, C.; Zhang, T.; Du, L.; Xie, L.; Zhu, J.; Chen, W.; Yang, R.; et al. Wafer-Scale Growth and Transfer of Highly-Oriented Monolayer MoS_2 Continuous Films. *ACS Nano* **2017**, *11*, 12001–12007.

(7) Chen, W.; Zhao, J.; Zhang, J.; Gu, L.; Yang, Z.; Li, X.; Yu, H.; Zhu, X.; Yang, R.; Shi, D.; Lin, X.; Guo, J.; Bai, X.; Zhang, G. Oxygen-Assisted Chemical Vapor Deposition Growth of Large Single-Crystal and High-Quality Monolayer MoS_2. *J. Am. Chem. Soc.* **2015**, *137*, 15632–15635.

(8) Gao, Y.; Liu, Z.; Sun, D.-M.; Huang, L.; Ma, L.-P.; Yin, L.-C.; Ma, T.; Zhang, Z.; Ma, X.-L.; Peng, L.-M.; Cheng, H.-M.; Ren, W. Large-Area Synthesis of High-Quality and Uniform Monolayer WS_2 on Reusable Au Foils. *Nat. Commun.* **2015**, *6*, 8569.

(9) Li, T.; Guo, W.; Ma, L.; Li, W.; Yu, Z.; Han, Z.; Gao, S.; Liu, L.; Fan, D.; Wang, Z.; Yang, Y.; Lin, W.; Luo, Z.; Chen, X.; Dai, N.; Tu, X.; Pan, D.; Yao, Y.; Wang, P.; Nie, Y.; et al. Epitaxial Growth of Wafer-Scale Molybdenum Disulfide

Semiconductor Single Crystals on Sapphire. *Nat. Nanotechnol.* **2021**, *16*, 1201–1207.

(10)Fu, J.-H.; Min, J.; Chang, C.-K.; Tseng, C.-C.; Wang, Q.; Sugisaki, H.; Li, C.; Chang, Y.-M.; Alnami, I.; Syong, W.-R.; Lin, C.; Fang, F.; Zhao, L.; Lo, T.-H.; Lai, C.-S.; Chiu, W.-S.; Jian, Z.-S.; Chang, W.-H.; Lu, Y.-J.; Shih, K.; et al. Oriented Lateral Growth of Two-Dimensional Materials on c-Plane Sapphire. *Nat. Nanotechnol.* **2023**, *18*, 1289–1294.

(11)Wang, J.; Xu, X.; Cheng, T.; Gu, L.; Qiao, R.; Liang, Z.; Ding, D.; Hong, H.; Zheng, P.; Zhang, Z.; Zhang, Z.; Zhang, S.; Cui, G.; Chang, C.; Huang, C.; Qi, J.; Liang, J.; Liu, C.; Zuo, Y.; Xue, G.; et al. Dual-Coupling-Guided Epitaxial Growth of Wafer-Scale Single-Crystal WS_2 Monolayer on Vicinal *a*-Plane Sapphire. *Nat. Nanotechnol.* **2022**, *17*, 33–38.

(12)Hoang, A. T.; Hu, L.; Kim, B. J.; Van, T. T. N.; Park, K. D.; Jeong, Y.; Lee, K.; Ji, S.; Hong, J.; Katiyar, A. K.; Shong, B.; Kim, K.; Im, S.; Chung, W. J.; Ahn, J.-H. Low-Temperature Growth of MoS_2 on Polymer and Thin Glass Substrates for Flexible Electronics. *Nat. Nanotechnol.* **2023**, *18*, 1439–1447.

(13)Chubarov, M.; Choudhury, T. H.; Hickey, D. R.; Bachu, S.; Zhang, T.; Sebastian, A.; Bansal, A.; Zhu, H.; Trainor, N.; Das, S.; Terrones, M.; Alem, N.; Redwing, J. M. Wafer-Scale Epitaxial Growth of Unidirectional WS_2 Monolayers on Sapphire. *ACS Nano* **2021**, *15*, 2532–2541.

(14)Liu, M.; Liao, J.; Liu, Y.; Li, L.; Wen, R.; Hou, T.; Ji, R.; Wang, K.; Xing, Z.; Zheng, D.; Yuan, J.; Hu, F.; Tian, Y.; Wang, X.; Zhang, Y.; Bachmatiuk, A.; Rümmeli, M. H.; Zuo, R.; Hao, Y. Periodical Ripening for MOCVD Growth of Large 2D Transition Metal Dichalcogenide Domains. *Adv. Funct. Mater.* **2023**, *33*, 2212773.

(15)Kang, K.; Xie, S.; Huang, L.; Han, Y.; Huang, P. Y.; Mak, K. F.; Kim, C.-J.; Muller, D.; Park, J. High-Mobility Three-Atom-Thick Semiconducting Films with Wafer-Scale Homogeneity. *Nature* **2015**, *520*, 656–660.

(16)Mun, J.; Park, H.; Park, J.; Joung, D.; Lee, S.-K.; Leem, J.; Myoung, J.-M.; Park, J.; Jeong, S.-H.; Chegal, W.; Nam, S.; Kang, S.-W. High-Mobility MoS_2 Directly Grown on Polymer Substrate with Kinetics-Controlled Metal–Organic Chemical Vapor Deposition. *ACS Appl. Electron. Mater.* **2019**, *1*, 608–616.

(17)Schaefer, C. M.; Caicedo Roque, J. M.; Sauthier, G.; Bousquet, J.; Hébert, C.; Sperling, J. R.; Pérez-Tomás, A.; Santiso, J.; del Corro, E.; Garrido, J. A. Carbon Incorporation in MOCVD of MoS_2 Thin Films Grown from an Organosulfide Precursor. *Chem. Mater.* **2021**, *33*, 4474–4487.

(18)Kim, T. S.; Dhakal, K. P.; Park, E.; Noh, G.; Chai, H.-J.; Kim, Y.; Oh, S.; Kang, M.; Park, J.; Kim, J.; Kim, S.; Jeong, H. Y.; Bang, S.; Kwak, J. Y.; Kim, J.; Kang, K. Gas-Phase Alkali Metal-Assisted MOCVD Growth of 2D Transition Metal Dichalcogenides for Large-Scale Precise Nucleation Control. *Small* **2022**, *18*, e2106368.

(19)Zhang, K.; Bersch, B. M.; Zhang, F.; Briggs, N. C.; Subramanian, S.; Xu, K.; Chubarov, M.; Wang, K.; Lerach, J. O.; Redwing, J. M.; Fullerton-Shirey, S. K.; Terrones, M.; Robinson, J. A. Considerations for Utilizing Sodium Chloride in Epitaxial Molybdenum Disulfide. *ACS Appl. Mater. Interfaces* **2018**, *10*, 40831–40837.

(20)Kim, H.; Ovchinnikov, D.; Deiana, D.; Unuchek, D.; Kis, A. Suppressing Nucleation in Metal-Organic Chemical Vapor Deposition of MoS_2 Monolayers by Alkali Metal Halides. *Nano Lett.* **2017**, *17*, 5056–5063.

(21)Cohen, A.; Patsha, A.; Mohapatra, P. K.; Kazes, M.; Ranganathan, K.; Houben, L.; Oron, D.; Ismach, A. Growth-Etch Metal-Organic Chemical Vapor Deposition Approach of WS_2 Atomic Layers. *ACS Nano* **2021**, *15*, 526–538.

(22)Park, J.-H.; Lu, A.-Y.; Shen, P.-C.; Shin, B. G.; Wang, H.; Mao, N.; Xu, R.; Jung, S. J.; Ham, D.; Kern, K.; Han, Y.; Kong, J. Synthesis of High-Performance Monolayer Molybdenum Disulfide at Low Temperature. *Small Methods* **2021**, *5*, e2000720.

(23)Zhu, J.; Park, J.-H.; Vitale, S. A.; Ge, W.; Jung, G. S.; Wang, J.; Mohamed, M.; Zhang, T.; Ashok, M.; Xue, M.; Zheng, X.; Wang, Z.; Hansryd, J.; Chandrakasan, A. P.; Kong, J.; Palacios, T. Low-Thermal-Budget Synthesis of Monolayer Molybdenum Disulfide for Silicon Back-End-of-Line Integration on a 200 Mm Platform. *Nat. Nanotechnol.* **2023**, *18*, 456–463.

(24)Wang, Q.; Li, N.; Tang, J.; Zhu, J.; Zhang, Q.; Jia, Q.; Lu, Y.; Wei, Z.; Yu, H.; Zhao, Y.; Guo, Y.; Gu, L.; Sun, G.; Yang, W.; Yang, R.; Shi, D.; Zhang, G. Wafer-Scale Highly Oriented Monolayer MoS_2 with Large Domain Sizes. *Nano Lett.* **2020**, *20*, 7193–7199.

(25)Wang, S.; Rong, Y.; Fan, Y.; Pacios, M.; Bhaskaran, H.; He, K.; Warner, J. H. Shape Evolution of Monolayer MoS_2 Crystals Grown by Chemical Vapor Deposition. *Chem. Mater.* **2014**, *26*, 6371–6379.

(26)Sebastian, A.; Pendurthi, R.; Choudhury, T. H.; Redwing, J. M.; Das, S. Benchmarking Monolayer MoS_2 and WS_2 Field-Effect Transistors. *Nat. Commun.* **2021**, *12*, 693.

(27)Dorow, C. J.; O'Brien, K. P.; Naylor, C. H.; Lee, S.; Penumatcha, A.; Hsiao, A.; Tronic, T.; Christenson, M.; Maxey, K.; Zhu, H.; Oni, A.; Alaan, U. S.; Gosavi, T. A.; Sen Gupta, A.; Bristol, R.; Clendenning, S.; Metz, M.; Avci, U. E. Advancing

Monolayer 2D NMOS and PMOS Transistor Integration From Growth to van Der Waals Interface Engineering for Ultimate CMOS Scaling. In *2021 Symposium on VLSI Technology*; IEEE, 2021; pp 1–2.

(28) Lin, Y.; Shen, P.-C.; Su, C.; Chou, A.-S.; Wu, T.; Cheng, C.-C.; Park, J.-H.; Chiu, M.-H.; Lu, A.-Y.; Tang, H.-L.; Tavakoli, M. M.; Pitner, G.; Ji, X.; McGahan, C.; Wang, X.; Cai, Z.; Mao, N.; Wang, J.; Wang, Y.; Tisdale, W.; et al. Contact Engineering for High-Performance N-Type 2D Semiconductor Transistors. In *2021 IEEE International Electron Devices Meeting (IEDM)*; IEEE, 2021; p 37.2.1-37.2.4.

(29) Shen, P.-C.; Su, C.; Lin, Y.; Chou, A.-S.; Cheng, C.-C.; Park, J.-H.; Chiu, M.-H.; Lu, A.-Y.; Tang, H.-L.; Tavakoli, M. M.; Pitner, G.; Ji, X.; Cai, Z.; Mao, N.; Wang, J.; Tung, V.; Li, J.; Bokor, J.; Zettl, A.; Wu, C.-I.; et al. Ultralow Contact Resistance between Semimetal and Monolayer Semiconductors. *Nature* **2021**, *593*, 211–217.

(30) Wan, Y.; Li, E.; Yu, Z.; Huang, J.-K.; Li, M.-Y.; Chou, A.-S.; Lee, Y.-T.; Lee, C.-J.; Hsu, H.-C.; Zhan, Q.; Aljarb, A.; Fu, J.-H.; Chiu, S.-P.; Wang, X.; Lin, J.-J.; Chiu, Y.-P.; Chang, W.-H.; Wang, H.; Shi, Y.; Lin, N.; et al. Low-Defect-Density WS_2 by Hydroxide Vapor Phase Deposition. *Nat. Commun.* **2022**, *13*, 4149.

(31) Jin, L.; Koester, S. J. High-Performance Dual-Gated Single-Layer WS_2 MOSFETs With Bi Contacts. *IEEE Electron Device Lett.* **2022**, *43*, 639–642.

(32) Li, M.-Y.; Hsu, C.-H.; Shen, S.-W.; Chou, A.-S.; Lin, Y. C.; Chuu, C.-P.; Yang, N.; Chou, S.-A.; Huang, L.-Y.; Cheng, C.-C.; Woon, W.-Y.; Liao, S.; Wu, C.-I.; Li, L.-J.; Radu, I.; Wong, H.-S. P.; Wang, H. Wafer-Scale Bi-Assisted Semi-Auto Dry Transfer and Fabrication of High-Performance Monolayer CVD WS_2 Transistor. In *2022 IEEE Symposium on VLSI Technology and Circuits (VLSI Technology and Circuits)*; IEEE, 2022; pp 290–291.

(33)Shi, X.; Li, X.; Guo, Q.; Gao, H.; Zeng, M.; Han, Y.; Yan, S.; Wu, Y. Improved Self-Heating in Short-Channel Monolayer WS_2 Transistors with High-Thermal Conductivity BeO Dielectrics. *Nano Lett.* **2022**, *22*, 7667–7673.

(34)Sun, Z.; Pang, C.-S.; Wu, P.; Hung, T. Y. T.; Li, M.-Y.; Liew, S. L.; Cheng, C.-C.; Wang, H.; Wong, H.-S. P.; Li, L.-J.; Radu, I.; Chen, Z.; Appenzeller, J. Statistical Assessment of High-Performance Scaled Double-Gate Transistors from Monolayer WS_2. *ACS Nano* **2022**, *16*, 14942–14950.

(35)Shi, X.; Li, X.; Guo, Q.; Zeng, M.; Wang, X.; Wu, Y. Ultrashort Channel Chemical Vapor Deposited Bilayer WS_2 Field-Effect Transistors. *Appl. Phys. Rev.* **2023**, *10*, 011405.

(36)Choi, S. H.; Kim, H.-J.; Song, B.; Kim, Y. I.; Han, G.; Nguyen, H. T. T.; Ko, H.; Boandoh, S.; Choi, J. H.; Oh, C. S.; Cho, H. J.; Jin, J. W.; Won, Y. S.; Lee, B. H.; Yun, S. J.; Shin, B. G.; Jeong, H. Y.; Kim, Y.-M.; Han, Y.-K.; Lee, Y. H.; et al. Epitaxial Single-Crystal Growth of Transition Metal Dichalcogenide Monolayers via the Atomic Sawtooth Au Surface. *Adv. Mater.* **2021**, *33*, e2006601.

(37)Zhou, S.; Liu, L.; Cui, S.; Ping, X.; Hu, D.; Jiao, L. Fast Growth of Large Single-Crystalline WS_2 Monolayers via Chemical Vapor Deposition. *Nano Res.* **2021**, *14*, 1659–1662.

(38)Yang, H.; Wang, Y.; Zou, X.; Bai, R.; Wu, Z.; Han, S.; Chen, T.; Hu, S.; Zhu, H.; Chen, L.; Zhang, D. W.; Lee, J. C.; Lu, X.; Zhou, P.; Sun, Q.; Yu, E. T.; Akinwande, D.; Ji, L. Wafer-Scale Synthesis of WS_2 Films with In Situ Controllable p-Type Doping by Atomic Layer Deposition. *Research* **2021**, *2021*, 9862483.